

Is Chaotic Advection Inherent to Heterogeneous Darcy Flow?

Daniel R. Lester^{1†}, Michael G. Trefry²
Guy Metcalfe³, Marco Dentz⁴

¹School of Engineering, RMIT University, Melbourne, Australia

²Independent Researcher, Perth, Australia

³Swinburne University of Technology, Melbourne, Australia

⁴Spanish National Research Council (IDAEA-CSIC), 08034 Barcelona, Spain

(Received ?; revised ?; accepted ?. - To be entered by editorial office)

At all scales, porous materials stir interstitial fluids as they are advected, leading to complex distributions of matter and energy. Of particular interest is whether porous media naturally induce chaotic advection at the Darcy scale, as these stirring kinematics profoundly impact basic processes such as solute transport and mixing, colloid transport and deposition and chemical, geochemical and biological reactivity. While many studies report complex transport phenomena characteristic of chaotic advection in heterogeneous Darcy flow, it has also been shown that chaotic dynamics are prohibited in a large class of Darcy flows. In this study we rigorously establish that chaotic advection is inherent to steady 3D Darcy flow in all realistic models of heterogeneous porous media. Anisotropic and heterogeneous 3D hydraulic conductivity fields generate non-trivial braiding of streamlines, leading to both chaotic advection and (purely advective) transverse dispersion. We establish that steady 3D Darcy flow has the same topology as unsteady 2D flow, and so use braid theory to establish a quantitative link between transverse dispersivity and Lyapunov exponent in heterogeneous Darcy flow. We show that chaotic advection and transverse dispersion occur in both anisotropic weakly heterogeneous and in heterogeneous weakly anisotropic conductivity fields, and that the quantitative link between these phenomena persists across a broad range of conductivity anisotropy and heterogeneity. The ubiquity of macroscopic chaotic advection has profound implications for the myriad of processes hosted in heterogeneous porous media and calls for a re-evaluation of transport and reaction methods in these systems.

Key words: Darcy flow, porous media, chaotic advection, topological braiding

1. Introduction

Porous media abound in both nature and engineered systems. From biological tissues to geological media and engineered materials, these media encompass a vast range of applications (Bear 1972; Cushman 2013). Porous materials play host to a range of fluid-borne phenomena, including mixing (Villermaux 2012; Dentz *et al.* 2023), dispersion (Saffman 1959; Bear 1972; Gelhar & Axness 1983; Dagan 1989), transport (Brenner & Edwards 1993) and reaction (de Anna *et al.* 2013; Rolle & Le Borgne 2019; Valocchi *et al.* 2019) of colloids, chemical and biological species (Alonso-Matilla *et al.* 2019; Dentz

† Email address for correspondence: daniel.lester@rmit.edu.au

et al. 2022). These phenomena are governed by the Lagrangian kinematics of the interstitial fluid, which provide an *advective template* that organises the spatial structures upon which they play out. At all scales, porous materials act to stir fluids as they are advected through (Villermaux 2012; Dentz *et al.* 2023), leading to highly striated material distributions which can have profound impacts upon these fluid-borne phenomena.

For example, solute mixing and transport can be either significantly accelerated or retarded by the Lagrangian kinematics of the flow, leading to the existence of e.g. isolated fast or slow mixing regions and transport “barriers” or “highways” (Haller 2015; Wu *et al.* 2024). Similarly, the kinetics of reactive solutes are governed by transport and mixing, including the formation of reaction “hot spots” due to localised fluid deformation (Rolle & Le Borgne 2019; Valocchi *et al.* 2019). It is impossible to understand, quantify and predict these processes without resolving their underlying Lagrangian kinematics (Metcalfe *et al.* 2023).

One important class of such kinematics is *chaotic advection* (Arnol’d 1965; Aref 1984) where fluid stirring motions (stretching and folding) yield highly striated distributions of matter and energy that can fundamentally alter these fluid-borne phenomena (Aref *et al.* 2017). For example, solute mixing is singular under chaotic advection (Cerbelli *et al.* 2017; Fereday & Haynes 2004) in that scalar dissipation persists in the limit of vanishingly small molecular diffusivity. Similarly, chaotic advection qualitatively augments both longitudinal (Jones & Young 1994) and transverse dispersion (Lester *et al.* 2014). Colloidal transport is also strongly augmented by chaotic advection, leading to formation of particle traps, repellers and deposition hot spots on fluid boundaries (Ouellette *et al.* 2008; Haller & Sapsis 2008). Chaotic advection also fundamentally alters chemical reactions (Tél *et al.* 2005; Neufeld & Hernandez-Garcia 2009) and biological activity (Tél *et al.* 2000; Károlyi *et al.* 2000), leading, e.g., singularly enhanced kinetics, coexistence of competitive species and altered stability characteristics. Hence, detection and quantification of chaotic advection in porous media flows is key to understanding, prediction and upscaling the myriad fluidic processes hosted in porous media.

Chaotic advection is inherent to steady three-dimensional (3D) pore-scale flow. It is now firmly established (Lester *et al.* 2013, 2016; Turuban *et al.* 2018, 2019; Kree & Villermaux 2017; Souzy *et al.* 2020; Heyman *et al.* 2021) that pore-scale chaotic advection arises in almost all porous media, ranging from granular matter to open pore networks. At the Darcy scale, chaotic advection has been predicted or observed in both natural (Trefry *et al.* 2019; Wu *et al.* 2020; Metcalfe *et al.* 2023; Wu *et al.* 2024) and engineered (Cho *et al.* 2019; Metcalfe *et al.* 2010; Mays & Neupauer 2012) transient Darcy flows. However chaotic advection has not been explicitly detected under steady 3D Darcy flow, despite consistent observations of complex Lagrangian kinematics (Chiogna *et al.* 2014; Ye *et al.* 2015). Conversely, several recent studies (Lester *et al.* 2021, 2022) have firmly established that chaotic dynamics cannot occur under steady 3D Darcy flow with smooth (C^1 -continuous) isotropic hydraulic conductivity fields. As such, the prevalence and nature of chaotic advection in steady heterogeneous Darcy flow is not understood.

In this study we rigorously establish that chaotic advection is inherent to all steady Darcy flows that are generated by faithful representations of heterogeneous porous media. This is important as most porous media are inherently heterogeneous at the Darcy scale (Bear 1972; Cushman 2013), and solute transport at this scale is typically advection dominated (Delgado 2007; Bear 1972), hence chaotic advection profoundly impacts solute transport, mixing and reactions. We consider the simplest non-trivial system of steady 3D Darcy flow arising from a mean potential gradient in unbounded systems with smooth, finite hydraulic conductivity fields. Although this precludes systems with stagnation points, non-smooth conductivity fields or impermeable inclusions, our focus

here is to understand basic Darcy flow. We establish that chaotic advection arises in the simplest physically plausible heterogeneous conductivity structures, even for weakly heterogeneous porous materials. Conversely strongly heterogeneous porous media exhibits a Lyapunov exponent close to the theoretical upper bound for steady 3D flow. We elucidate the underlying mechanisms and establish a quantitative link between the strength of chaotic mixing and (purely advective) transverse dispersion. Application of this link to experimental dispersion data also indicates chaotic mixing is significant and ubiquitous in heterogeneous Darcy flow.

This work is organized as follows. In §2 we show that all realistic models of heterogeneous media must have anisotropic hydraulic conductivity fields. The braiding of streamlines in Darcy flow and the connection with chaotic advection are then considered in §3, including development of a quantitative link between transverse dispersion and Lyapunov exponent in random braiding flows. Numerical simulations are performed in §4, including anisotropic Darcy flow with variable heterogeneity and heterogeneous Darcy with varying anisotropy. In §5 the mechanisms generating chaotic advection in Darcy flow and implications for solute mixing are discussed. Conclusions are given in §6.

2. Kinematics of Porous Media Flows

2.1. Kinematics of Pore and Darcy Scale Flow

We first consider the kinematics of steady 3D pore-scale flow before upscaling to Darcy flow. Steady 3D pore scale flow is described by the Stokes equations

$$\mu \nabla^2 \hat{\mathbf{v}}(\mathbf{x}) - \nabla \hat{p}, \quad \nabla \cdot \hat{\mathbf{v}} = 0, \quad \mathbf{x} \in \Omega_f, \quad (2.1)$$

subject to no-slip conditions $\hat{\mathbf{v}}|_{\partial\Omega_{fs}} = \mathbf{0}$ at the pore boundary $\partial\Omega_{fs}$. Here $\hat{\mathbf{v}}$ is the pore-scale velocity, \hat{p} the pore-scale pressure field, Ω_f , Ω_s respectively are the fluid (pore) and solid (grain) domains. For steady 3D flow, the topological complexity of the boundary $\partial\Omega_{fs}$ generates pore-scale chaotic advection (Lester *et al.* 2013). Upscaling by suitably averaging of (2.1) (denoted by $\langle \cdot \rangle_p$) yields the Darcy equation (Bear 1972)

$$\mathbf{v}(\mathbf{x}) = -\mathbf{K}(\mathbf{x}) \cdot \nabla \phi(\mathbf{x}), \quad \nabla \cdot \mathbf{v} = 0, \quad \mathbf{x} \in \Omega, \quad (2.2)$$

where $\Omega \equiv \langle \Omega_f \cup \Omega_s \rangle_p$ denotes the Darcy-scale porous medium, $\mathbf{v} \equiv \langle \hat{\mathbf{v}} \rangle_p$ is the (upscaled) Darcy-scale velocity, $\phi \equiv \langle \hat{p} \rangle_p$ the upscaled potential field, and $\mathbf{K}(\mathbf{x})$ is the hydraulic conductivity tensor field that captures viscous drag due to no-slip conditions on $\partial\Omega_{fs}$.

As this pore boundary generates chaotic advection, omission of $\partial\Omega_{fs}$ in (2.2) via upscaling also omits these pore-scale kinematics, the effects of which must be incorporated via coarse-grained models of, e.g., solute mixing, dispersion and reaction. Hence homogeneous Darcy flow (i.e. $\mathbf{K}(\mathbf{x}) = \text{const.}$) is non-chaotic at the Darcy scale while the pore-scale flow is chaotic. In this study we focus solely on heterogeneous conductivity fields as these represent the majority of porous media (Bear 1972; Cushman 2013).

2.2. Kinematics of Heterogeneous Darcy Flow

For most porous materials the hydraulic conductivity tensor $\mathbf{K}(\mathbf{x})$ is anisotropic due to anisotropy of the underlying pore-scale structure, which occurs in, e.g., stratified formations in geological media and structured engineered media (Bear 1972). Under conventional upscaling approaches the conductivity tensor $\mathbf{K}(\mathbf{x})$ (a second rank tensor) is symmetric and positive definite (Bear 1972), with six independent components in 3D space which vary spatially in heterogeneous formations but are all assumed to be smooth, continuous and finite. Hence $\mathbf{K}(\mathbf{x})$ may be locally diagonalized into principal directions

with three independent components as $\mathbf{K}'(\mathbf{x}) = \mathbf{R}(\mathbf{x}) \cdot \mathbf{K}(\mathbf{x}) \cdot \mathbf{R}^{-1}(\mathbf{x})$, where $\mathbf{R}(\mathbf{x})$ is a rotation tensor field and

$$\mathbf{K}'(\mathbf{x}) \equiv \begin{pmatrix} K'_{11}(\mathbf{x}) & 0 & 0 \\ 0 & K'_{22}(\mathbf{x}) & 0 \\ 0 & 0 & K'_{33}(\mathbf{x}) \end{pmatrix}. \quad (2.3)$$

Even if $\mathbf{R}(\mathbf{x})$ is spatially invariant, this conductivity field is fundamentally anisotropic if one of the diagonal components $K'_{ii}(\mathbf{x})$ differs from the others.

Conversely, many studies (Beaudoin & de Dreuzy 2013; Boon *et al.* 2016; Chaudhuri & Sekhar 2005; Dartois *et al.* 2018; Delgado 2007; Gelhar & Axness 1983; Janković *et al.* 2009; Neuman & Zhang 1990), consider the hydraulic conductivity tensor to be isotropic as $\mathbf{K}(\mathbf{x}) = k(\mathbf{x})\mathbf{I}$, where $k(\mathbf{x}) = K'_{ii}(\mathbf{x})$ for $i = 1 : 3$, and (2.2) simplifies to

$$\mathbf{v}(\mathbf{x}) = -k(\mathbf{x})\nabla\phi, \quad \nabla \cdot \mathbf{v} = 0, \quad \mathbf{x} \in \Omega. \quad (2.4)$$

The kinematics of isotropic Darcy flow markedly differ from that of anisotropic Darcy flow. If $k(\mathbf{x})$ is smooth and \mathbf{v} does not admit stagnation points, then isotropic Darcy flow only admits simple kinematics because the helicity density $\mathcal{H}(\mathbf{x}) \equiv \mathbf{v} \cdot (\nabla \times \mathbf{v})$ is identically zero

$$\mathcal{H}(\mathbf{x}) = k\nabla\phi \cdot (\nabla\phi \times \nabla k) = 0, \quad (2.5)$$

regardless of the heterogeneity of $k(\mathbf{x})$. The total helicity $H \equiv \int_{\Omega} \mathcal{H}(\mathbf{x})d\mathbf{x}$ over the domain Ω is a topological invariant that characterises the topological complexity (knottedness) of vortex lines of the flow (Woltjer 1958; Moreau 1961; Moffatt 1969), and the helicity-free condition $H = 0$ precludes chaotic dynamics in steady 3D flows (Arnol'd 1965). Hence steady 3D isotropic Darcy flows are non-chaotic and *integrable* and so admit two invariants ψ_1, ψ_2 that act as orthogonal streamfunctions (Lester *et al.* 2022; Yoshida 2009), leading to the Euler velocity representation

$$\mathbf{v}(\mathbf{x}) = \nabla\psi_1(\mathbf{x}) \times \nabla\psi_2(\mathbf{x}), \quad \nabla\psi_1(\mathbf{x}) \cdot \nabla\psi_2(\mathbf{x}) = 0. \quad (2.6)$$

Streamlines of isotropic Darcy flow are confined to the intersections of streamsurfaces given by level sets of $\psi_1(\mathbf{x}), \psi_2(\mathbf{x})$. Such confinement prohibits transverse dispersion in the purely advective limit $Pe \rightarrow \infty$ (henceforth simply termed transverse dispersion), regardless of medium heterogeneity (Lester *et al.* 2023).

These kinematic constraints are illustrated in Figure 1c, which shows typical streamlines for isotropic Darcy flow with strongly heterogeneous ($\sigma_{\ln K}^2 = 4$) hydraulic conductivity. Although the streamlines are highly tortuous due to heterogeneity of the medium, they do not exhibit asymptotic transverse dispersion. In §4.1 the transverse dispersivity of this flow is numerically computed to be effectively zero.

These kinematic constraints persist even if the scalar field $k(\mathbf{x})$ is *statistically* anisotropic (i.e. has different correlation structures in different principal directions), as the corresponding Darcy flow is still locally isotropic and $\mathcal{H} = 0$. We remark on the application of these results to the so-called ‘‘helicity paradox’’ (Cirpka *et al.* 2015) that occurs when a statistically anisotropic but locally isotropic conductivity field is upscaled from the Darcy scale to the block field scale, resulting in an anisotropic block-scale conductivity field (Bear 1972). This spuriously adds degrees of freedom to the Lagrangian kinematics and permits block-scale chaotic advection where none should exist based on the fully resolved Darcy scale flow. While beyond the scope of this paper, our results highlight the need for upscaling methods that obey the appropriate kinematic constraints.

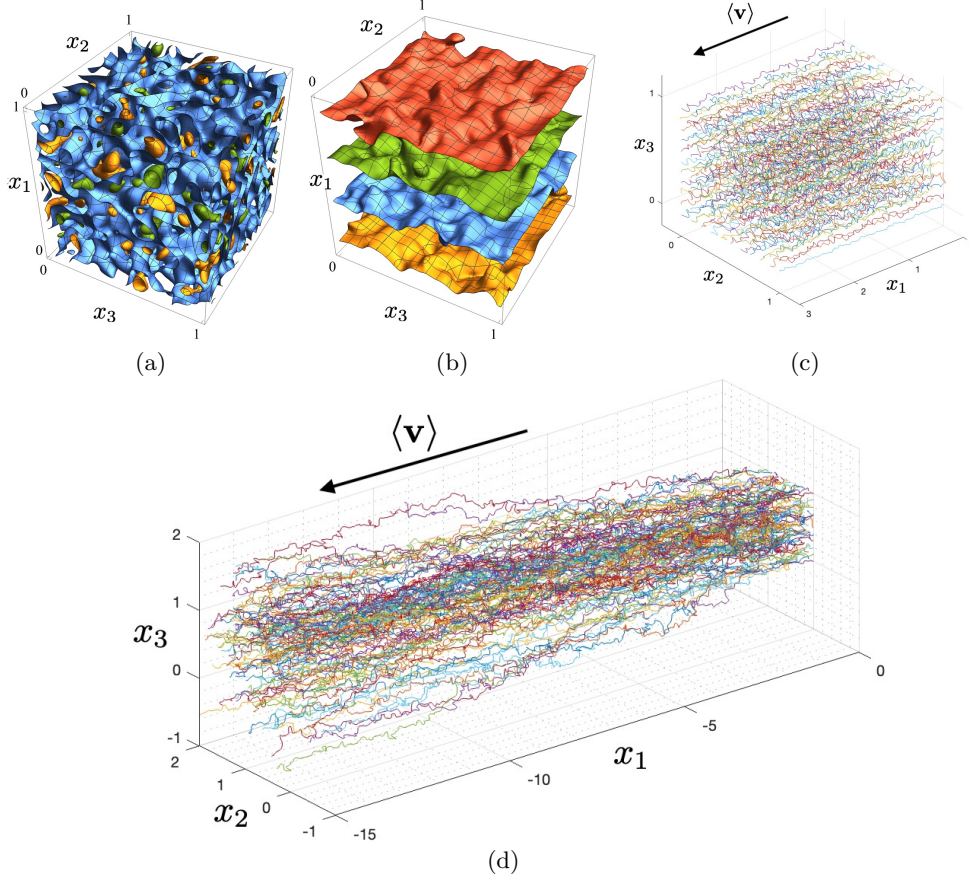


FIGURE 1. (a) Isosurfaces of the typical normalised heterogeneous log-conductivity field $f(\mathbf{x}) = \ln K(\mathbf{x})/\sigma_{\ln K}^2$ used to model isotropic $k(\mathbf{x})\mathbf{I}$ and anisotropic $\mathbf{K}(\mathbf{x})$ conductivity tensors and (b) associated potential field $\phi(\mathbf{x})$ for anisotropic Darcy flow driven by a uniform mean potential gradient. Associated streamlines for heterogeneous Darcy flow with (c) isotropic conductivity field ($\delta = 0$ in (4.1)) and (d) anisotropic conductivity field ($\delta = 1$ in (4.1)) with log-conductivity variance $\sigma_{\ln K}^2 = 4$ and parameters $N = 4$, $N_i = 2$ in (4.2).

2.3. Implications for Hydraulic Conductivity Modelling

These results question the validity of isotropic Darcy flow (2.4) as a model for heterogeneous porous systems; indeed experimental observations clearly show that transverse dispersion is non-zero toward the purely advective limit $Pe \rightarrow \infty$ (Delgado 2007; Hackert *et al.* 1996). Although several numerical studies (Beaudoin & de Dreuzy 2013; Dartois *et al.* 2018; Janković *et al.* 2009) have found that isotropic Darcy flow can generate purely advective transverse dispersion, these observations arise in systems with either non-smooth conductivity fields or impermeable inclusions, or from numerical schemes that violate the kinematic constraints associated with (2.6). Numerical schemes that implicitly enforce these constraints yield zero transverse dispersivity (Lester *et al.* 2023).

Conversely, anisotropic conductivity fields $\mathbf{K}(\mathbf{x})$ generate non-zero helicity density

$$\mathcal{H}(\mathbf{x}) = (\mathbf{K} \cdot \nabla \phi) \cdot (\nabla \times \mathbf{K} \cdot \nabla \phi) \neq 0, \quad (2.7)$$

and non-zero total helicity $H \neq 0$. Hence the streamlines of anisotropic Darcy flow are no longer constrained to the streamsurfaces of $\psi_1(\mathbf{x})$, $\psi_2(\mathbf{x})$, but rather freely wander

through the medium (Lester *et al.* 2023), thereby giving rise to persistent transverse dispersion. This behaviour is shown in Figure 1d, where the streamlines associated with strongly heterogeneous ($\sigma_{\ln K}^2 = 4$) anisotropic Darcy flow transversely spread throughout the flow domain as they are advected longitudinally. In §4.1 the transverse dispersivity D_T of this flow is quantitatively shown to be non-zero.

Note that non-zero helicity density $\mathcal{H}(\mathbf{x}) \neq 0$ is not sufficient to ensure non-zero transverse dispersivity. The classical Clebsch 3D vector field parameterization into the smooth continuous scalar fields $\alpha_1(\mathbf{x})$, $\beta_1(\mathbf{x})$, $\varphi(\mathbf{x})$

$$\mathbf{v}(\mathbf{x}) = \alpha_1(\mathbf{x})\nabla\beta_1(\mathbf{x}) + \nabla\varphi(\mathbf{x}) \quad \mathbf{x} \in \Omega, \quad (2.8)$$

has been found to be incomplete (Yoshida 2009), meaning that some 3D vector fields cannot be represented by (2.8). Yoshida & Morrison (2017) classify flows conforming to (2.8) as *epi-2D* flows (topologically 2D) with non-zero helicity density $\mathcal{H}(\mathbf{x}) \neq 0$ but are helicity free, $H = 0$. Conversely, only 3D velocity fields given by the complete Clebsch parameterization (Yoshida 2009)

$$\mathbf{v}(\mathbf{x}) = \sum_{i=1}^2 \alpha_i(\mathbf{x})\nabla\beta_i(\mathbf{x}) + \nabla\varphi(\mathbf{x}), \quad (2.9)$$

have non-zero total helicity H and so admit chaotic advection. Conversely, realistic heterogeneous conductivity models yield 3D velocity fields of the form (2.9) that admit chaotic advection and transverse dispersion.

To summarise, realistic hydraulic conductivity models of heterogeneous porous media must be anisotropic to be consistent with experimental observations (Delgado 2007; Hackert *et al.* 1996) of non-zero transverse dispersion in the purely advective limit $Pe \rightarrow \infty$. As non-zero transverse dispersion requires $H \neq 0$, this raises the potential for chaotic advection, which is inevitable in nonlinear continuous systems with arbitrary coefficients and three degrees of freedom (dof=3) (Speetjens *et al.* 2021). In the following section we firmly establish that transverse dispersion and chaotic advection are intimately linked in heterogeneous Darcy flow.

3. Streamline Braiding and Chaos

3.1. Topology of 2D Unsteady and 3D Steady Flows

The link between dispersion and chaotic mixing can be explored via consideration of streamline braiding. As 1D streamlines are invariants of steady 3D flow, *braiding* of streamlines stirs the fluid continuum in a complex manner, as shown in Figure 2a. This concept has been used to quantify stirring in another 3 dof system – unsteady 2D flow – where non-trivial braiding of 1D pathlines can stretch and fold the fluid continuum as shown in Figure 2a. For unsteady 2D flow, braid group theory (Boyland *et al.* 2000; Handel & Thurston 1985; Moussafr 2006) has been developed to quantify the topological entropy h_{braid} of the path-line braiding motions, closely related to the Lyapunov exponent λ_∞ (Thiffeault 2005). Below we show that 2D unsteady flow is topologically equivalent to steady 3D Darcy flow, hence this mathematical framework applies to these flows.

The topology of steady 3D flow $\mathbf{v}(\mathbf{x}) = [v_1(\mathbf{x}), v_2(\mathbf{x}), v_3(\mathbf{x})]$ with one unidirectional velocity component (e.g., $v_3(\mathbf{x}) > 0$) can be equated (Bajer 1994) to that of unsteady 2D flow via the rescaling $\mathbf{v}'(\mathbf{x}) = \mathbf{v}(\mathbf{x})/v_3(\mathbf{x})$ such that the x_3 coordinate acts as an analogue for time. For strongly heterogeneous 3D Darcy flows this transformation breaks down when $v_3(\mathbf{x})$ is zero or negative due to flow reversal in the vicinity of low permeability structures. However, these flows are still fundamentally unidirectional as the potential

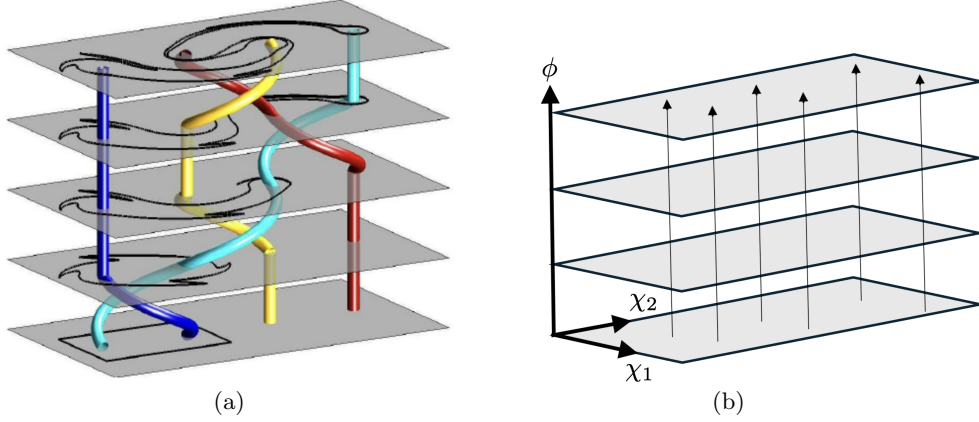


FIGURE 2. (a) Schematic of streamline (or pathline) braiding in a unidirectional steady 3D flow (or unsteady 2D flow). The set of four thick coloured streamlines (or pathlines) braid with each other as they evolve with the mean flow direction x_3 (or time t). This topological braiding motion stirs the fluid continuum (grey planes) and the length of the black rectangular material boundary grows exponentially with the number of braiding motions. Adapted from Thiffeault & Finn (2006). This schematic also depicts streamline braiding in steady 3D anisotropic Darcy flow with intrinsic coordinates $\xi = (\chi_1, \chi_2, \phi)$, where the grey planes depict isopotential surfaces. (b) Absence of braiding in isotropic Darcy flow in intrinsic coordinates $\xi = (\chi_1, \chi_2, \phi)$. As the velocity field is everywhere orthogonal to level sets of ϕ denoted by grey planes, streamlines in this coordinate system do not move laterally or undergo braiding.

field $\phi(\mathbf{x})$ is strictly monotonic decreasing along streamlines $\nabla\phi(\mathbf{x}) \cdot \mathbf{v}(\mathbf{x}) = -\nabla\phi(\mathbf{x}) \cdot \mathbf{K}(\mathbf{x}) \cdot \nabla\phi(\mathbf{x}) < 0$ due to the positive definite nature of $\mathbf{K}(\mathbf{x})$ (Bear 1972). This leads to the intrinsic coordinate basis $\xi = (\chi_1, \chi_2, \phi)$, where χ_1, χ_2 are orthogonal to ϕ , and the representation $\mathbf{v}_\xi(\xi) = [v_{\chi_1}(\xi), v_{\chi_2}(\xi), v_\phi(\xi)]$ with $v_\phi(\xi) > 0$. Thus, the velocity field $\mathbf{v}_\xi(\xi)$ may be rescaled as

$$\mathbf{v}'_\xi(\xi) = \left[\frac{v_{\chi_1}(\xi)}{v_\phi(\xi)}, \frac{v_{\chi_2}(\xi)}{v_\phi(\xi)}, 1 \right], \quad v_\phi(\xi) > 0 \forall \xi \in \Omega. \quad (3.1)$$

This velocity field is topologically equivalent to that of unsteady 2D flow, and the isopotential surfaces of steady 3D Darcy flow (Figure 1b) are analogous to isochrones of unsteady 2D flow. Hence streamlines in steady 3D Darcy flow are topologically equivalent to pathlines of unsteady 2D flow and the mathematical framework developed for pathline braiding can be directly applied to steady 3D Darcy flow. As per Figure 2b, the representation (3.1) also shows directly that isotropic Darcy flow cannot generate streamline braiding, where $(\chi_1, \chi_2) = (\psi_1, \psi_2)$ and (3.1) simplifies to $\mathbf{v}'_\xi(\xi) = (0, 0, 1)$ because the velocity field is everywhere orthogonal to the level sets of ϕ , i.e. $\mathbf{v} \times \nabla\phi = \mathbf{0}$. These streamlines do not move relative to each other in the isopotential surfaces $\phi = \text{const.}$, let alone undergo non-trivial braiding motions. In Cartesian coordinates (Figure 1c), the helicity-free condition constrains non-braiding yet tortuous streamlines to streamsurfaces $\psi_1(\mathbf{x}) = \text{const.}$, $\psi_2(\mathbf{x}) = \text{const.}$

Conversely, anisotropic Darcy flow admits non-zero transverse velocity components $v_{\chi_1}(\xi), v_{\chi_2}(\xi)$ and so streamlines can undergo the braiding motions as shown in Figure 2a and Figure 1d. Although transverse motion of streamlines in the (χ_1, χ_2) directions does not necessarily generate non-trivial braiding, below we show that non-trivial braiding is inherent to steady random 3D flows.

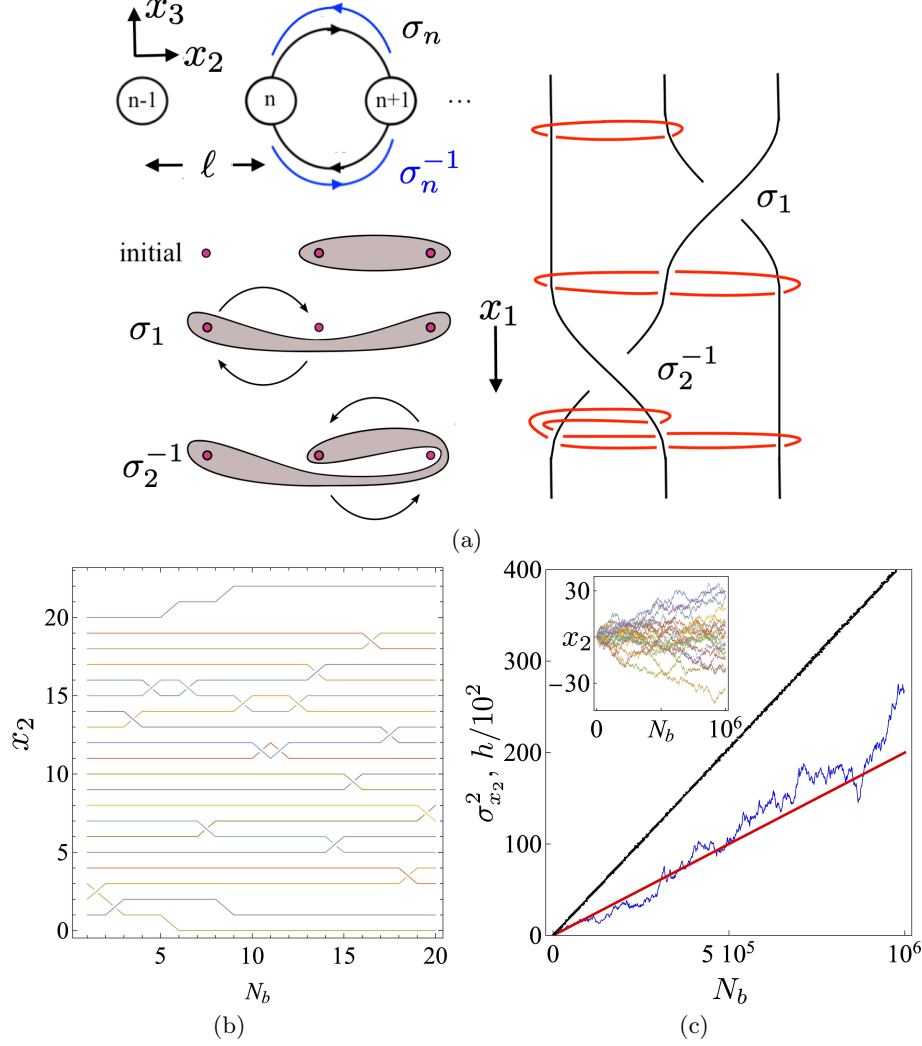


FIGURE 3. (a) Top left: schematic of streamlines $n-1$, n , $n+1$ in the transverse x_2-x_3 plane with clockwise (black) σ_n , anti-clockwise (blue) σ_n^{-1} braid generators in the 1D streamline model. Bottom left: stretching of material elements due to braiding motions (adapted from Thiffeault (2022)) that evolve in the longitudinal ϕ direction. Right: braid diagram (black) depicting stretching of material elements (red) as braid evolves in longitudinal ϕ direction. (b) Braid diagram depicting evolution of x_2 coordinate of $N_p = 20$ streamlines over $N_b = 20$ random braid actions in the longitudinal ϕ direction, leading to non-trivial braiding and dispersion of streamlines. (c) Growth of topological entropy h (black line) and transverse variance $\sigma_{x_2}^2$ (blue line) with braid number N_b , which agrees well with theory (Lester *et al.* 2024) (red line). Inset: Brownian motion of streamlines due to streamline braiding with braid number N_b . Adapted from Lester *et al.* (2024).

3.2. Topological Complexity of 3D Streamline Braiding

Braid group theory is used to quantify stirring in unsteady 2D flows (Boyland *et al.* 2000) via a well-developed mathematical framework (Artin 1947; Moussafir 2006; Thiffeault 2022) that efficiently encodes fluid stirring via a symbolic braiding representation of the topology of pathlines in spacetime. This encoding can be used to compute the topological complexity of their braiding motions, and the Neilson-Thurston classifica-

tion theorem (Handel & Thurston 1985) characterises braids as periodic, reducible or pseudo-Anosov types, the latter of which is interpreted as an indicator of chaotic dynamics (Boyland *et al.* 2000). Due to topological equivalence, this framework can also be applied to streamline braiding in steady 3D Darcy flow.

For steady unidirectional 3D flow, streamline braiding is encoded via a sequence of *braid generators* $\sigma_n^{\pm 1}$ (Artin 1947). As shown in Figure 3a, braiding of streamlines (circles) in the (x_2, x_3) plane of \mathbb{R}^3 space can be characterised in terms of the “crossing” of these streamlines with respect to arbitrary reference direction x_3 as they propagate unidirectionally in the x_1 direction (into the page in Figure 3a). Note streamlines are labelled $(\dots, n-1, n, n+1, \dots)$ with respect to their relative position in the x_2 coordinate, hence these labels are updated after each crossing event. The braid generators σ_n and σ_n^{-1} respectively characterise clockwise and counter-clockwise crossing of streamlines n and $n+1$. An ordered sequence of braid generators form the *braid word* $\mathbf{b} = \sigma_{n_1}^{\pm 1} \sigma_{n_2}^{\pm 1} \dots$, which is determined by the sequence of streamline crossings in the x_1 direction. As shown in Figure 3a (bottom left and right), these braiding motions act to stretch and fold fluid elements (brown), leading to exponential stretching if they are of pseudo-Anosov type.

The topological entropy \hat{h} of a dynamical system measures the rate of loss of information of the system about its initial conditions. For fluid flows \hat{h} is closely related to the largest infinite-time Lyapunov exponent $\hat{\lambda}_\infty$ and forms an upper bound for $\hat{\lambda}_\infty$ (Thiffeault 2010). In practice, the topological entropy of a flow can be interpreted as the asymptotic exponential growth rate of the length $l(t)$ of a material line (Newhouse & Pignataro 1993) as

$$\hat{h} = \lim_{t \rightarrow \infty} \frac{1}{t} \ln \frac{l(t)}{l(0)}. \quad (3.2)$$

For ergodic flows such as purely hyperbolic steady 3D flow (which has a single positive Lyapunov exponent), the upper bound given by the topological entropy is exact (Yomdin 1987; Newhouse 1988; Newhouse & Pignataro 1993; Matsuoka & Hiraide 2015; Catalan 2019), i.e.

$$\hat{h} = \hat{\lambda}_\infty. \quad (3.3)$$

Conversely, many studies dating over half a century (Villermaux 2019; Duplat *et al.* 2010; Kalda 2000; Hinch 1999; Girimaji & Pope 1990; Cocke 1969) propose that as fluid elements undergo stretching, the relative length $\rho \equiv \delta l(t)/\delta l(0)$ of infinitesimal line elements is distributed log-normally with log-mean $\hat{\lambda}_\infty t$ and log-variance $\hat{\sigma}_\lambda^2 t$. In §4.2 and Appendix C we confirm that an *ab initio* derivation of fluid stretching in steady 3D flows yields the same result if the velocity distribution does not yield anomalous transport. For this scenario a reasonable conclusion (Villermaux 2019; Duplat *et al.* 2010; Hinch 1999) is that the growth rate of $l(t) = \int_0^{l(0)} \delta l(t)/\delta l(0) dl$ is given by the ensemble average of ρ , which, via (3.2), yields

$$\hat{h} = \hat{\lambda}_\infty + \frac{\sigma_\lambda^2}{2}. \quad (3.4)$$

as the variance of $\ln \rho$ contributes to the growth of $\ln l(t)$. However, the discrepancy of (3.4) with (3.3) has recently been explained by Lester & Dentz (2024), who show that in the asymptotic limit, temporal sampling of the finite-time Lyapunov exponent $\hat{\lambda}(\mathbf{X}, t)$ (which converges to $\hat{\lambda}_\infty$ as σ_λ/\sqrt{t}) dominates over the ensemble average represented by (3.4), yielding (3.3). In §5.1 we show that heterogeneous Darcy flow with random stationary conductivity $\mathbf{K}(\mathbf{x})$ is ergodic and purely hyperbolic (i.e. it does not admit non-hyperbolic features such as elliptic or parabolic Lagrangian Coherent Structures).

The dimensionless topological entropy $h \equiv \hat{h}\ell/\langle v_1 \rangle$ (with velocity correlation length ℓ) may be approximated by considering the topological entropy h_{braid} of the braid word \mathbf{b} of a set of streamlines of the flow. The braid entropy h_{braid} characterises the asymptotic growth (with number of braiding motions $k = t\langle v_1 \rangle/\ell$) of the number of *distinguishable orbits* of the braid (Thiffeault 2022). For steady 3D flow this may be interpreted as the number of distinct linkages that a material line (e.g. Figure 3a) makes if it is fully contracted until it forms a *loop* ℓ_E that tightly contacts these streamlines. The topological entropy h_{braid} of a braid word \mathbf{b} is then

$$h_{\text{braid}} = \lim_{k \rightarrow \infty} \frac{1}{k} \log \frac{|\mathbf{b}^k \ell_E|}{|\ell_E|}, \quad (3.5)$$

where the metric $|\cdot|$ measures the number of linkages of the braid. Although non-trivial, various methods (Moussafir 2006; Hall & Yurttaş 2009; Thiffeault 2022) are available to rigorously compute h_{braid} from a given braid word \mathbf{b} . As the braid entropy h_{braid} only considers the complexity of streamline braiding, it forms a lower bound for h , however for many systems it converges to h with increasing number N_p of streamlines as

$$\lim_{N_p \rightarrow \infty} h_{\text{braid}} \rightarrow h = \lambda_\infty. \quad (3.6)$$

Hence for heterogeneous Darcy flow both the topological entropy h and dimensionless Lyapunov exponent $\lambda_\infty \equiv \hat{\lambda}_\infty \ell / \langle v_1 \rangle$ may be accurately estimated from the braid entropy h_{braid} of a sufficiently large set of streamlines.

3.3. Linking Dispersion and Chaos in Streamline Braiding Flows

Lester *et al.* (2024) recently examined the link between chaotic advection and transverse dispersion in randomly braiding flows via a simple 1D streamline model. As per Figure 3a (top left), this model consists of a set of N_p streamlines in \mathbb{R}^3 space that repeat periodically in the transverse x_2 direction and propagate due to mean flow in the longitudinal x_1 direction. These streamlines have the same x_3 -coordinate ($x_3 = 0$) and uniform spacing $\Delta x_2 = \ell$ in the x_2 -direction, corresponding to the velocity correlation length scale ℓ . At integer multiples of longitudinal distance Δ_L , one pair $(n, n+1)$ of neighbouring streamlines randomly exchange position in the $x_2 - x_3$ plane via clockwise or counter-clockwise rotations, as labelled by the respective braid generators σ_n, σ_n^{-1} .

The streamline braiding motions are defined by a braid word \mathbf{b} comprised of N_b braid generators $\mathbf{b} = \sigma_{n_1}^{\pm 1} \sigma_{n_2}^{\pm 1} \dots \sigma_{n_{N_b}}^{\pm 1}$ which is constructed by randomly choosing each generator from the set $\{\sigma_1, \sigma_1^{-1}, \dots, \sigma_{N_p}, \sigma_{N_p}^{-1}\}$. Streamlines undertake an unbounded random walk along the x_2 coordinate as they propagate longitudinally (Figure 3c, inset), while deforming the interstitial fluid (Figure 3a, right). The topological braid entropy h_{braid} of these motions is efficiently computed via the *braidlab* package (Thiffeault & Budišić 2013–2021). Figure 3b shows the braid diagram for a typical braid word \mathbf{b} consisting of $N_p = 20$ streamlines and $N_b = 20$ braid generators. Figure 3c shows linear growth of topological braid entropy h_{braid} and transverse variance $\sigma_{x_2}^2$ of this system with N_b .

Lester *et al.* (2024) show that the topological braid entropy h_{braid} and transverse variance $\sigma_{x_2}^2$ of this system grow linearly with N_b , and in the limit of large N_b and N_p , the scaled mean topological braid entropy $\langle h_{\text{braid}} \rangle$ for 10^3 realizations of this simple 1D streamline model converges to the *random braid entropy* $\langle \lambda_\sigma \rangle$ as

$$\lim_{N_p \rightarrow \infty} \lim_{N_b \rightarrow \infty} \langle h_{\text{braid}} \rangle \frac{N_p}{N_b} \rightarrow \langle \lambda_\sigma \rangle \approx 0.8529, \quad (3.7)$$

leading to a simple relationship between λ_∞ and the transverse dispersivity $D_T \equiv$

$\lim_{t \rightarrow \infty} d/dt \sigma_{x_2}^2/2$ as

$$\lambda_\infty = \frac{\langle \lambda_\sigma \rangle}{Pe_T}, \quad (3.8)$$

where $Pe_T \equiv \ell \langle v_1 \rangle / D_T$ is the transverse Péclet number.

Two different 2D extensions of this 1D streamline model were also considered by Lester *et al.* (2024); one involving a 2D streamline array analogous to the 1D array in Figure 3a, and another involving 3D streamlines that undertake independent random walks constructed by making a jump of fixed magnitude by random orientation in the $x_2 - x_3$ plane at regular intervals in the x_1 coordinate. For both of these models the appropriately scaled topological braid entropy h_{braid} was also found to converge to the random braid entropy $\langle \lambda_\sigma \rangle$, leading to a simple relationship between the Lyapunov exponent λ_∞ of the flow and the transverse Péclet number Pe_T as

$$\lambda_\infty^d = \langle \lambda_\sigma \rangle^d \left(\frac{\ell}{\Delta_L} \right)^{d-1} \frac{d}{Pe_T}, \quad (3.9)$$

where $d = 1, 2$ is the Euclidean dimension of the streamline array. The persistence of this relationship across these diverse models suggests that they all belong to the same *universality class* (Ódor 2004) associated with streamline braiding. This establishes that chaotic advection and transverse dispersion are intimately linked in heterogeneous Darcy flow because they are both driven by non-trivial streamline braiding. Equation (3.9) also points to development of methods to estimate λ_∞ from transverse dispersivity data for specific systems, however further research is required to extend this link to non-ideal systems.

3.4. Fluid Deformation in Heterogeneous Darcy Flow

In addition to streamline braiding, it is also instructive to consider *ab initio* evolution of fluid deformation in heterogeneous Darcy flow from a kinematic perspective. This can be quantified by considering deformation as a random process. Le Borgne *et al.* (2008a,b) established that for steady flow in random media, the velocity magnitude v decorrelates with distance s along streamlines and is described by a spatial Markov process with respect to spatial correlation length ℓ . It has also been shown (Lester *et al.* 2022) that the velocity gradient in steady Darcy flow is also spatially Markovian, hence fluid deformation is characterised by sampling the dimensionless velocity gradient tensor $\epsilon(t; \mathbf{X}) \equiv \nabla \mathbf{v}(\mathbf{x}(t; \mathbf{X}))^\top \ell / \langle v_1 \rangle$ equidistantly with distance s along streamlines. Rotation into the *Protean* coordinate frame \mathbf{x}' (Lester *et al.* 2018a) renders the velocity gradient tensor $\epsilon'(t; \mathbf{X})$ upper triangular (see Appendix B for details) and the fluid deformation gradient tensor $\mathbf{F}'(t; \mathbf{X})$ which evolves as

$$\frac{d\mathbf{F}'(t; \mathbf{X}')}{dt} = \epsilon'(t; \mathbf{X}) \cdot \mathbf{F}'(t; \mathbf{X}), \quad \mathbf{F}'(0; \mathbf{X}) = \mathbf{1}, \quad (3.10)$$

is likewise. The diagonal elements F'_{ii} represent principal stretches and the off-diagonal components F'_{ij} (non-zero for $j > i$) represent shear deformations. Hence the hyperbolic stretches that govern the Lyapunov exponents are given by the diagonal components ϵ'_{ii} , and are not conflated with shear deformations given by the off-diagonal components ϵ'_{ij} . From (3.10), the diagonal elements of $\mathbf{F}'(t; \mathbf{X})$ grow exponentially as

$$F'_{ii}(t; \mathbf{X}') = \exp \left[\int_0^t dt' \epsilon'_{ii}(t'; \mathbf{X}) \right], \quad i = 1, 2, 3, \quad (3.11)$$

From (3.11), fluid stretching in the streamwise direction simply fluctuates with the local velocity as $F'_{11}(t) = v(t)/v(0)$, hence $\langle \epsilon'_{11}(t) \rangle = 0$. As $\sum_i \epsilon'_{ii} = 0$ for divergence free flow

flows, the Lyapunov exponent is then

$$\lambda_\infty = \langle \epsilon'_{22} \rangle = -\langle \epsilon'_{33} \rangle, \quad (3.12)$$

where $\langle \cdot \rangle$ denotes spatial averaging along streamlines. Hence $F'_{22} \sim \exp(\lambda_\infty t)$ and $F'_{33} \sim \exp(-\lambda_\infty t)$, and so chaotic advection in steady 3D flow is characterised by the single Lyapunov exponent λ_∞ .

In Appendix C we show that (3.11) leads to an *ab initio* continuous time random walk (CTRW) for the relative stretch $\rho \equiv \delta l(\mathbf{X}, t)/\delta l(\mathbf{X}, 0)$ of infinitesimal fluid line elements along streamlines as

$$\begin{aligned} \ln \rho_{n+1} &= \ln \rho_n + \frac{\ell \epsilon_n}{v_n}, \\ t_{n+1} &= t_n + \tau_n = t_n + \frac{\ell}{v_n}, \\ s_{n+1} &= s_n + \ell, \end{aligned} \quad (3.13)$$

where v_n and τ_n respectively are the streamline velocity magnitude and advection time between s_n and s_{n+1} and ϵ_n is the relevant Protean velocity gradient component ϵ'_{22} . The distribution $\psi(\tau)$ of waiting times τ is related to the Lagrangian velocity distribution $p_s(v)$ as

$$\psi(\tau) = \frac{\ell p_s(\ell/\tau)}{\tau^2}, \quad (3.14)$$

and $p_s(v) = v p_e(v)/\langle v \rangle_e$ (Dentz *et al.* 2016), where $p_e(v)$ is the Eulerian velocity distribution and $\langle \cdot \rangle_e$ represents an Eulerian average. For heterogeneous Darcy flow the Lagrangian velocity distribution may be heavy-tailed in the small velocity limit (Berkowitz *et al.* 2006), i.e., $p_s(v) \propto v^{\beta-1}$, $\beta > 1$ for $v \ll \langle v \rangle$ depending on the distribution of hydraulic conductivity (Hakoun *et al.* 2019). Thus, the waiting time distribution scales as

$$\psi(\tau) \approx \frac{\psi_0}{|\Gamma(-\beta)|} t^{-1-\beta} \quad \text{for } \tau/\langle \tau \rangle \gg 1, \quad (3.15)$$

and the q -th order moments $\langle \tau^q \rangle$ of $\psi(\tau)$ are finite for $q < \lfloor \beta \rfloor$. Hence normal transport arises if $\beta > 2$, as the mean and variance of $\psi(\tau)$ are bounded, but anomalous transport arises for $1 < \beta < 2$ as the variance of $\psi(\tau)$ is unbounded. For $\beta > 1$, the advection time t_n may be related to the number of increments n as

$$t_n = \sum_{i=1}^n \tau_i \approx n \langle \tau \rangle = n \ell \left\langle \frac{1}{v_n} \right\rangle = \frac{n \ell}{\langle v \rangle_e} = n \tau_c, \quad (3.16)$$

where $\tau_c \equiv \ell/\langle v \rangle_e$ is the mean transition time. Similarly, the mean of $\ln \rho$ also grows linearly in time as $\langle \ln \rho \rangle = \langle \epsilon_n \rangle t = \lambda_\infty t$. The rate of growth of the variance $\sigma_{\ln \rho}^2$ serves as an important input parameter for lamellar mixing theories (Le Borgne *et al.* 2015; Villiermaux 2019) that predict evolution of the concentration PDF for advective-diffusive solute transport from fluid stretching behaviour. Dentz *et al.* (2015) and Rebenshtok *et al.* (2014) show that in the asymptotic limit the coupled CTRW (3.13) generates q -th order absolute central moments μ_q for $q > \beta$ which scale as

$$\mu_q(t) \equiv \lim_{t \rightarrow \infty} \langle |\ln \rho - \lambda_\infty t|^q \rangle \sim \begin{cases} t^{1+q-\beta} & \text{for } 1 < \beta < 2, \\ t^{q/2} & \text{for } \beta > 2, \end{cases} \quad (3.17)$$

hence anomalous transport ($\beta < 2$) in heterogeneous 3D Darcy flow can also generate anomalous stretching dynamics. In Appendix C we show for the case $\beta > 2$, $p_{\ln \rho}(\ln \rho)$

converges to a normal distribution with mean and variance

$$\lim_{t \rightarrow \infty} \langle \ln \rho \rangle = \lambda_\infty t \quad \lim_{t \rightarrow \infty} \sigma_{\ln \rho}^2 = \sigma_\lambda^2 t, \quad (3.18)$$

where $\sigma_\lambda^2 \equiv \sigma_\epsilon^2 \langle \tau^2 \rangle / \tau_c$ and σ_ϵ^2 is the variance of $p_\epsilon(\epsilon)$. For the anomalous stretching case ($1 < \beta < 2$), the variance $\sigma_{\ln \rho}^2$ growth ranges from normal to ballistic as (Dentz *et al.* 2015)

$$\lim_{t \rightarrow \infty} \sigma_{\ln \rho}^2 = \frac{\psi_0 \beta \Gamma(\beta + 1)}{6 - 5\beta + \beta^2} t^{3-\beta}. \quad (3.19)$$

Under such anomalous stretching the equality (3.3) between h and λ_∞ persists as temporal averaging along streamlines still dominates (Lester & Dentz 2024), but convergence of (3.2) slows as $\beta \downarrow 1$ and physical processes such as mixing and dispersion may be impacted in this limit. In §4, we find that the flows considered herein all exhibit normal transport. However, anomalous stretching dynamics form an important kinematic regime that warrants future investigation.

4. Chaotic Advection in Heterogeneous Darcy Flow

4.1. Onset of Chaotic Advection with Anisotropy

The results in §3 uncover a deep link between chaotic advection and transverse dispersion in heterogeneous Darcy flow, and show how anomalous transport generates anomalous stretching dynamics. To examine the onset of chaotic advection with medium anisotropy, we first consider Darcy flow in the simplest possible conductivity field that admits non-zero helicity:

$$\mathbf{K}(\mathbf{x}) = k_0(\mathbf{x})\mathbf{I} + \delta[k_\delta(\mathbf{x}) - k_0(\mathbf{x})]\hat{\mathbf{e}}_1 \otimes \hat{\mathbf{e}}_1, \quad (4.1)$$

where $k_0(\mathbf{x}) \neq k_\delta(\mathbf{x})$ and $\delta \in [0, 1]$ quantifies anisotropy of the conductivity tensor. Although this flow has been previously considered (Lester *et al.* 2024) in the context of quantifying the link between stirring and dispersion, here we focus on the onset of chaotic dynamics with δ . Note that while similar conductivity tensor fields such as $\mathbf{K}(\mathbf{x}) = k_0(\mathbf{x})(\mathbf{I} + \delta\hat{\mathbf{e}}_1 \otimes \hat{\mathbf{e}}_1)$ have non-zero helicity density $\mathcal{H}(\mathbf{x}) \neq 0$, the resulting flows are shown (Appendix A to be epi-2D (Yoshida & Morrison 2017) and hence non-chaotic (Holm & Kimura 1991; Arnol'd 1965).

Darcy flow over the conductivity field (4.1) is driven by a unit potential gradient $\nabla\bar{\phi} = \{-1, 0, 0\}$ in a triply-periodic unit cube (3-torus \mathbb{T}^3) $\Omega : \mathbf{x} \in [0, 1] \times [0, 1] \times [0, 1]$, and the scalar log-conductivity fields $f(\mathbf{x}) \equiv \ln k(\mathbf{x})$ for the independent fields $k_0(\mathbf{x})$, $k_\delta(\mathbf{x})$ are given by

$$f(\mathbf{x}) = \Sigma_{\ln K}^2 \sum_{n=1}^{N_i} \sum_{i,j,k}^N \frac{A_{n,ijk}}{\sqrt{i^2 + j^2 + k^2}} \cos[2\pi i(x_1 + \chi_{n,ijk}^1)] \cos[2\pi j(x_2 + \chi_{n,ijk}^2)] \cos(2\pi k(x_3 + \chi_{n,ijk}^3)), \quad (4.2)$$

with $N = 4$ and so the velocity correlation length $\ell = 1/(2N)$. $N_i = 2$ is the number of realisations in each mode, and $A_{n,ijk}$ and $\chi_{n,ijk}^m$ with $m = 1, 2, 3$ are uniformly distributed random variables in $[0, 1]$. The coefficient $\Sigma_{\ln K}$ is chosen such that the log-variance of the conductivity field is $\|f^2\|_\Omega = \sigma_{\ln K}^2 = 4$. A typical scalar field $f(\mathbf{x})$ with these parameters is shown in Figure 1a. Note fields with $N = 1$ do not generate chaotic dynamics due to symmetry of the velocity field.

To solve the divergence-free condition $\nabla \cdot \mathbf{v} = 0$ over Ω , ϕ is decomposed into a mean

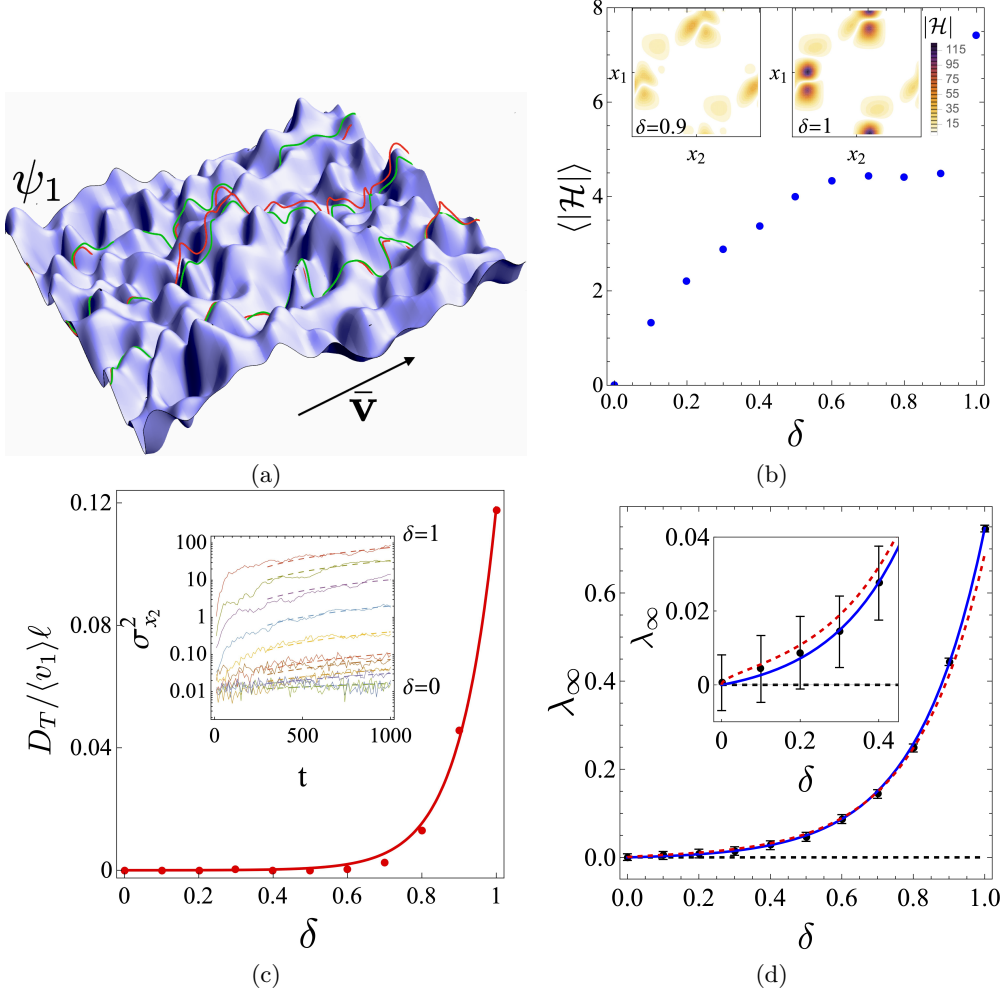


FIGURE 4. (a) Perturbation of $\delta = 0.1$ streamlines (red) from $\delta = 0$ (zero helicity) streamlines (green) and associated ψ_1 streamsurface (blue) for the conductivity field given in (4.1). Similar perturbation of $\delta = 0.1$ streamlines away from the ψ_2 streamsurfaces (not shown) also occurs. (b) Growth of mean absolute helicity $\langle |\mathcal{H}| \rangle$ with δ , inset shows $|\mathcal{H}|$ fields for $\delta = 0.9, 1$ (Adapted from (Lester *et al.* 2024)). (c) Growth of transverse dispersivity $D_T / \langle v_1 \rangle \ell$ with δ from simulations (red points) and fitted exponential (4.7) (red curve). Inset shows temporal evolution of transverse variance. (d) Growth of Lyapunov exponent λ_∞ with perturbation parameter δ from simulations (black points) and fitted exponential (4.8) (blue curve). (red dotted curve) dimensionless Lyapunov exponent λ_∞ predicted from fitted exponential in (b) and (3.9). (c), (d) Adapted from (Lester *et al.* 2024).

and fluctuation as

$$\phi(\mathbf{x}) = \bar{\phi}(\mathbf{x}) + \tilde{\phi}(\mathbf{x}), \quad (4.3)$$

where $\bar{\phi} = -x_1$. From (2.2), $\tilde{\phi}(\mathbf{x})$ is governed by

$$\nabla \cdot (\mathbf{K} \cdot \nabla \tilde{\phi}(\mathbf{x})) - \nabla \cdot (\mathbf{K} \cdot \hat{\mathbf{e}}_1) = 0. \quad (4.4)$$

Methods to solve (4.4) and perform streamline tracking are detailed in Appendix D, and typical potential fields and streamlines are shown in Figure 1. For each value of δ , a realization of $\mathbf{K}(\mathbf{x})$ is generated, (4.4) is solved and 10^3 3D streamlines are computed

for distance $10^4\ell$, along with the transverse dispersivity D_T , Protean velocity gradient tensor ϵ' and Lyapunov exponent $\lambda_\infty = \langle \epsilon'_{22} \rangle$, as described in Appendix C.

Typical streamfunctions $\psi_1(\mathbf{x})$, $\psi_2(\mathbf{x})$ for the helicity-free flow $\delta = 0$ given by (2.6) (see Appendix D for solution details) are shown in Figure 4a. Streamlines (red) are confined to the intersections of the level sets of ψ_1 and ψ_2 , and their global behaviour is shown in Figure 1c. Despite their significant tortuosity, these confined streamlines do not exhibit persistent dispersion or non-trivial braiding. Conversely, for $\delta > 0$ the associated streamlines (green) in Figure 4a are unconfined and so exhibit streamline braiding and transverse dispersion, see also Figure 1d for $\delta = 1$.

Figure 4b shows that the mean helicity magnitude $\langle |\mathcal{H}| \rangle$ increases from $\mathcal{H}(\mathbf{x}) = 0$ everywhere for $\delta = 0$ to a plateau $\langle |\mathcal{H}| \rangle \approx 4.74$ at $\delta = 0.9$, then suddenly increases to $\langle |\mathcal{H}| \rangle \approx 7.16$ at $\delta = 1$. This sharp increase as $\delta \uparrow 1$ is attributed to the loss of correlation between the K_{11} and $K_{22} = K_{33}$ fields. The linear growth of $\langle |\mathcal{H}| \rangle$ for $\delta \ll 1$ is explained by decomposing the potential field ϕ as $\phi(\mathbf{x}) = \phi_0(\mathbf{x}) + \delta \phi_\delta(\mathbf{x})$. To leading order $\mathbf{v}(\mathbf{x})$ is then

$$\begin{aligned} \mathbf{v}(\mathbf{x}) &= \mathbf{v}_0(\mathbf{x}) + \delta \mathbf{v}_\delta(\mathbf{x}), \\ &= -k_0 \nabla \phi_0 - \delta [k_0 \nabla \phi_\delta - k_\delta \hat{\mathbf{e}}_1 (\hat{\mathbf{e}}_1 \cdot \nabla \phi_0)] + \mathcal{O}(\delta^2), \end{aligned} \quad (4.5)$$

where $\mathbf{v}_0(\mathbf{x})$ is helicity-free and the helical perturbation $\mathbf{v}_\delta(\mathbf{x})$ is generated by the difference $k_0 - k_\delta$

$$\begin{aligned} \mathcal{H}(\mathbf{x}) &= \delta [k_0 \nabla \phi \cdot (\hat{\mathbf{e}}_1 \times \nabla (k_\delta - k_0) (\nabla \phi \cdot \hat{\mathbf{e}}_1)) \\ &\quad + (k_\delta - k_0) (\nabla \phi \cdot \hat{\mathbf{e}}_1 \otimes \hat{\mathbf{e}}_1 \cdot (\nabla k_0 \times \nabla \phi))] + \mathcal{O}(\delta^2). \end{aligned} \quad (4.6)$$

Figure 4c shows D_T increases exponentially with δ as

$$\frac{D_T}{\langle v_1 \rangle \ell} = \frac{1}{Pe_T} \approx 4.343 \times 10^{-6} (e^{10.214 \delta} - 1), \quad (4.7)$$

and (2.6) recovers $D_T = 0$ for $\delta = 0$ (Lester *et al.* 2023), indicating finite transverse dispersion arises for weak perturbations away from heterogeneous isotropic Darcy flow. Figure 4d shows that λ_∞ also increases exponentially with δ as

$$\lambda_\infty \approx 0.00381 (e^{5.283 \delta} - 1), \quad (4.8)$$

and is also non-zero for small $\delta > 0$, indicating that chaotic advection occurs for weak perturbations away from isotropic Darcy flow. For $\delta = 0$ the streamfunction formulation (2.6) enforces zero Lyapunov exponent (Lester *et al.* 2022). Figure 4d also shows that insertion of the fitted exponential (4.8) for D_T into (3.9) (assuming $\Delta_L = \ell$) yields excellent agreement with the measured Lyapunov exponent (4.7). This is unexpected as the domain Ω is finite and so does not belong to a universality class (Ódor 2004); however, these results indicate that the relationship (3.9) can also hold away from the limit $N_p = L/\ell \rightarrow \infty$. These results establish that chaotic advection is inherent to heterogeneous Darcy flow, even in the limit of weakly anisotropic media.

4.2. Onset of Chaotic Advection with Medium Heterogeneity

To examine the impact of medium heterogeneity upon anisotropic Darcy flow, we consider flow generated by the anisotropic diagonal conductivity tensor $\mathbf{K}(\mathbf{x})$ in (2.3), where the scalar conductivity fields K_{ii} are generated in the same manner as k_0 , k_δ but with $N_i = 4$. The heterogeneity of these fields K_{ii} is varied from weakly ($\sigma_{\ln K}^2 < 1$) to strongly ($\sigma_{\ln K}^2 > 1$) heterogeneous over the range of log-variances $\sigma_{\ln K}^2 = (2^{-10}, 2^{-8}, \dots, 2^{-2}) \cup (1/2, 1, 2, 3, 4)$. For each value of $\sigma_{\ln K}^2$, a realisation of $\mathbf{K}(\mathbf{x})$ is generated and (4.4) is

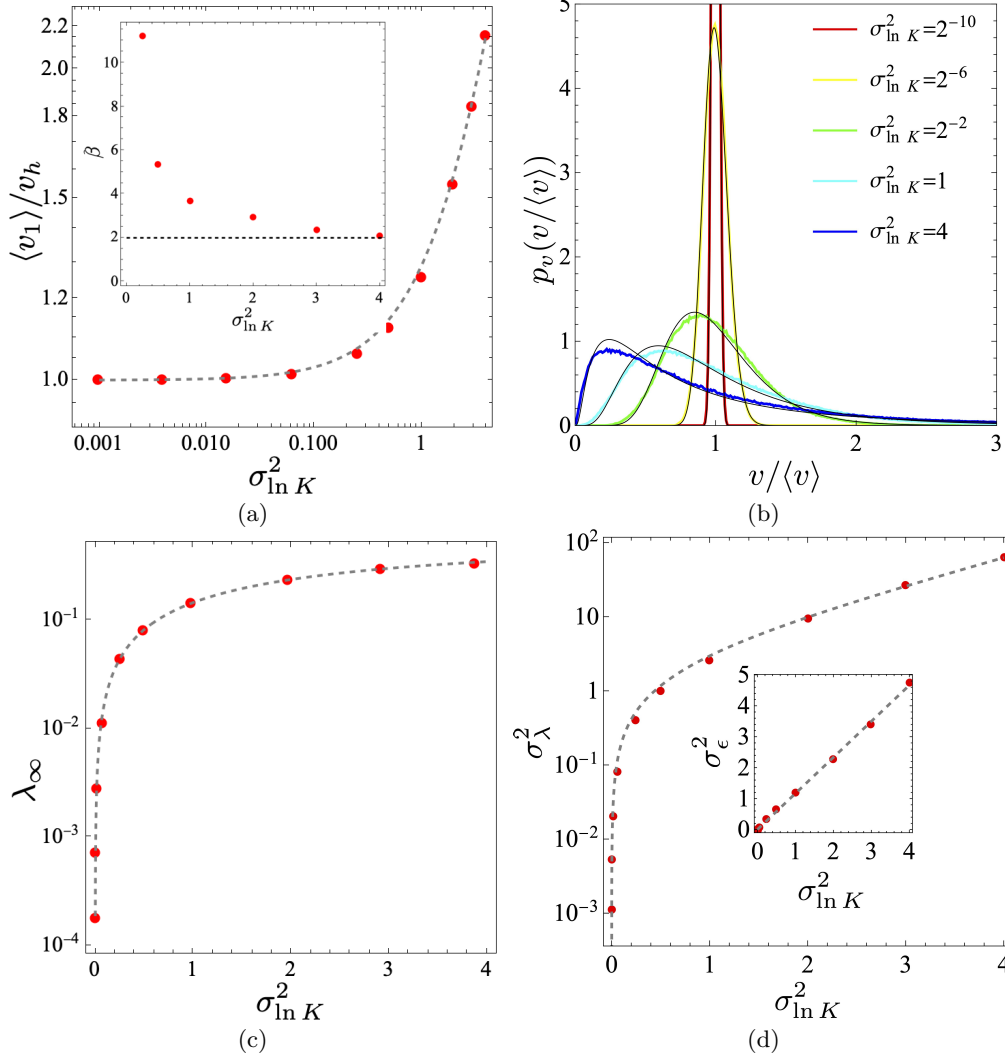


FIGURE 5. (a) Variation of normalised mean longitudinal velocity $\langle v_1 \rangle / v_h$ (red points) with log-variance $\sigma_{\ln K}^2$ and linear fit (4.9), (grey dashed line) in anisotropic Darcy flow. (Inset) Variation of small velocity scaling index β with $\sigma_{\ln K}^2$. (b) PDFs of normalised velocity magnitude $p_v(v/\langle v \rangle)$ as a function of log-variance $\sigma_{\ln K}^2$ and fitted log-normal distribution (black lines). (c) Variation of dimensionless Lyapunov exponent λ_∞ (red dots) with log-variance $\sigma_{\ln K}^2$ and nonlinear fit (4.14), (grey dashed line). (d) Variation of dimensionless stretching variance σ_λ^2 with log-variance $\sigma_{\ln K}^2$ and nonlinear fit (4.11), (grey dashed line). (Inset) Variation of Protean velocity gradient variance σ_ϵ^2 with log-variance $\sigma_{\ln K}^2$ and linear fit (4.10), (grey dashed line).

solved, and streamlines, D_T and λ_∞ are computed in the same manner as described in §4.1.

Figure 5a shows that the scaled mean longitudinal velocity $\langle v_1 \rangle / v_h$ (where v_h is the velocity for a homogeneous medium) increases linearly with log-variance $\sigma_{\ln K}^2$ as expected for small and moderate values of $\sigma_{\ln K}^2$ (Renard & De Marsily 1997)

$$\frac{\langle v_1 \rangle}{v_h} = 1 + \alpha_1 \sigma_{\ln K}^2, \quad (4.9)$$

with $\alpha_1 \approx 0.29178$ and coefficient of determination $R^2 = 0.999$. Figure 5b shows that the Eulerian velocity PDF $p_v(v)$ roughly follows a log-normal distribution for all but strongly heterogeneous flows, and converges toward a delta function in the homogeneous limit $\sigma_{\ln K}^2 \rightarrow 0$. For $\sigma_{\ln K}^2 \geq 1$, the velocity PDF scales as a power law in the small velocity limit as $p_v(v) \propto v^{\beta-1}$, and the inset in Figure 5a shows that the index $\beta > 2$ and approaches $\beta \downarrow 2$ in the strongly heterogeneous regime, leading to normal transport for all $\sigma_{\ln K}^2 \geq 1$. The persistence of normal transport in the strongly heterogeneous regime is attributed to the low probability of all three K_{ii} in (2.3) being simultaneously small. We also note that different random models such as Gamma-distributed conductivity fields have a greater propensity to generate anomalous transport (Hakoun *et al.* 2019).

Figure 5c shows that λ_∞ converges to a constant value with increasing log-variance $\sigma_{\ln K}^2$, and is well fitted by the simple nonlinear function (4.14) as described below. As shown in the inset of Figure 5d, the velocity gradient variance σ_ϵ^2 (from data presented in §4.3) grows linearly with conductivity log-variance as

$$\sigma_\epsilon^2 \approx \alpha_2 \sigma_{\ln K}^2, \quad (4.10)$$

where $\alpha_2 = 1.1656$ with $R^2 = 0.999$, and σ_λ^2 grows exponentially with $\sigma_{\ln K}^2$ as

$$\sigma_\lambda^2 \approx \alpha_3 \left(e^{\alpha_4 \sigma_{\ln K}^2} - 1 \right), \quad (4.11)$$

where $\alpha_3 = 2.2429$ and $\alpha_4 = 0.8415$ with $R^2 = 0.999$. These results show that although the Lyapunov exponent λ_∞ converges toward the upper bound $\ln 2$ with increasing medium heterogeneity, the corresponding variance σ_λ^2 increases due to growth of the second moment $\langle \tau^2 \rangle$. For the case of anomalous transport ($1 < \beta < 2$), this variance grows super-linearly as $\sigma_{\ln \rho}^2 \sim t^{3-\beta}$ Lester *et al.* (2018a).

In addition to direct computation of λ_∞ , the topological braid entropy h_{braid} of the streamlines is computed directly via the E-tec routine (Roberts *et al.* 2019), which is limited to moderately heterogeneous ($0.1 \leq \sigma_{\ln K}^2 \leq 2$) systems due to lack of convergence for $\sigma_{\ln K}^2 < 0.1$ and flow reversal for $\sigma_{\ln K}^2 > 1$. In principle, streamlines for the strongly heterogeneous cases could be placed in the intrinsic coordinates $\xi = (\chi_1, \chi_2, \phi)$, however, determination of χ_1, χ_2 is difficult as the non-zero helicity density $\mathcal{H}(\mathbf{x}) \neq 0$ means that mutual Lie derivatives of the flow do not vanish and so there does not exist an intrinsic *holonomic basis* (Schutz 1980) for (χ_1, χ_2) . Figure 6a shows that λ_∞ and h_{braid} agree to within 5%, verifying (3.3).

In the weakly heterogeneous regime ($\sigma_{\ln K}^2 \leq 1$), λ_∞ varies almost linearly with log-variance as

$$\lambda_\infty \approx (\sigma_{\ln K}^2)^{\alpha_5}, \quad (4.12)$$

with $\alpha_5 = 1.129$ and $R^2 = 0.995$, suggesting that chaotic advection arises in weakly heterogeneous anisotropic conductivity fields. Figure 6b shows that in the strongly heterogeneous regime, λ_∞ scales linearly with $\sigma_{\ln K}^2$ as

$$\lambda_\infty \frac{\langle v_1 \rangle}{v_h} \approx \alpha_6 \sigma_{\ln K}^2, \quad (4.13)$$

with $\alpha_6 \approx 0.198$ and $R^2 = 0.999$. As per Figure 5c, the behavior of λ_∞ as a function of $\sigma_{\ln K}^2$ can be fitted by

$$\lambda_\infty = \frac{\alpha_1 \sigma_{\ln K}^2}{1 + \alpha_6 \sigma_{\ln K}^2}, \quad (4.14)$$

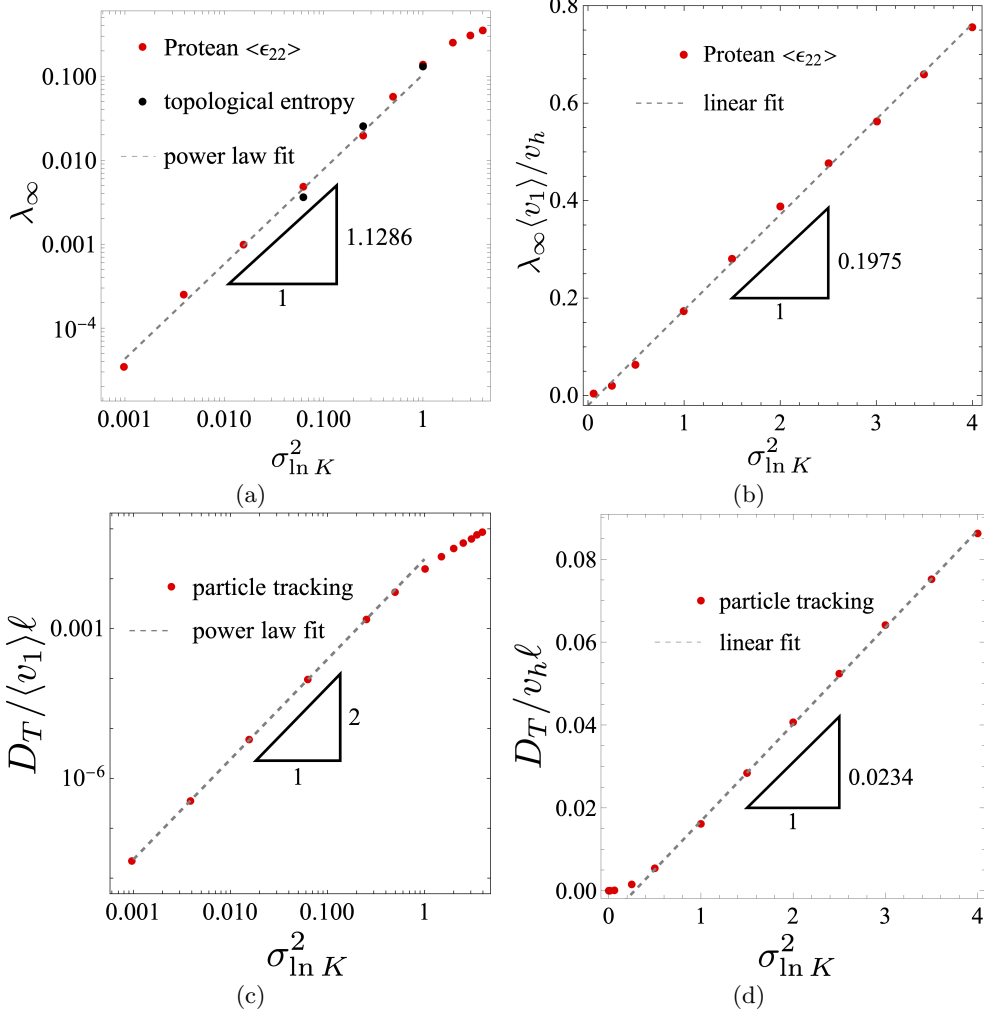


FIGURE 6. (top) Lyapunov exponents and (bottom) dispersion coefficients in (a, c) weakly ($\sigma_{\ln K}^2 \leq 1$) and (b,d) strongly ($\sigma_{\ln K}^2 \geq 1$) heterogeneous porous media with anisotropic conductivity given by (2.3). Red points in (a, b) indicate Lyapunov exponents computed from the Protean frame (Lester *et al.* 2018a), black points indicate topological entropy computed using E-tec (Roberts *et al.* 2019). Dashed lines in (a, c) and (b, d) respectively indicate power law (4.12), (4.16), and linear (4.13), (4.17), fits to the Lyapunov exponents and dispersion coefficients in the weakly and strongly heterogeneous regimes.

which implies that λ_∞ converges in the strongly heterogeneous limit

$$\lim_{\sigma_{\ln K}^2 \rightarrow \infty} \lambda_\infty \approx \frac{\alpha_1}{\alpha_6} = 0.677. \quad (4.15)$$

This value is close to the upper bound $h = \ln 2 \approx 0.693$ for steady 3D flow (Dinh & Sibony 2008), indicating strong chaotic mixing arises in strongly heterogeneous Darcy flow.

Convergence of λ_∞ in (4.15) is understood by considering the limit $\sigma_{\ln K}^2 \rightarrow \infty$ and partitioning \mathbf{K} over Ω into infinitely permeable Ω_∞ ($\text{tr } \mathbf{K}(\mathbf{x}) \rightarrow \infty$) and an impermeable Ω_0 ($\text{tr } \mathbf{K}(\mathbf{x}) \rightarrow 0$) subdomains. As Ω is the 3-torus \mathbb{T}^3 with topological genus $g = 3$, the boundary $\partial\Omega_{\infty 0}$ between the subdomains is also topologically complex and thus

admits saddle-type stagnation points \mathbf{x}_0 on $\partial\Omega_{\infty 0}$ as per the Poincaré-Hopf theorem. These saddle points generate chaotic advection via the same mechanism as for pore-scale Stokes flow (Lester *et al.* 2013). Due to the linearity of Darcy flow, the rescaled fluid velocity field $\mathbf{v}/\langle v_1 \rangle$ and associated saddle points and Lyapunov exponent are all invariant in the limit $\sigma_{\ln K}^2 \rightarrow \infty$.

Figure 6c shows that the transverse dispersivity scales nonlinearly in the weakly heterogeneous regime as

$$\frac{D_T}{\langle v_1 \rangle \ell} \sim (\sigma_{\ln K}^2)^{2.01}, \quad (4.16)$$

and linearly in the strongly heterogeneous regime as

$$\frac{D_T}{v_h \ell} \approx 0.0234 \sigma_{\ln K}^2, \quad (4.17)$$

with $R^2 = 1.000$ in both cases. In the weakly heterogeneous regime, the scalings of D_T (4.16) and λ_∞ (4.12) with $\sigma_{\ln K}^2$ agree with the relationship (3.9) linking dispersion and chaotic advection in random flows. However, as expected this relationship does not persist in the strongly heterogeneous regime due to the onset of flow reversal. These results establish that chaotic advection is inherent to anisotropic media, even in the limit of weakly heterogeneous conductivity fields.

4.3. Velocity Gradient Statistics

In addition to the Lyapunov exponent, the Protean velocity gradient $\boldsymbol{\epsilon}'$ provides important information regarding the deformation structure of heterogeneous Darcy flow. For all computed flows $\boldsymbol{\epsilon}'$ is sampled along 10^3 streamlines at fixed spatial increment ℓ for a distance of $10^4 \ell$. Figure 7(a,c) and (b,d) respectively show the PDFs of the principal stretches ϵ'_{ii} and shears ϵ'_{ij} for strongly heterogeneous ($\sigma_{\ln K}^2 = 4$) Darcy flow for (a,b) fully anisotropic ($\delta = 1$) and (c,b) isotropic ($\delta = 0$) conductivity fields (4.1). For all flows computed the divergence error $|\sum_{i=1}^3 \epsilon'_{ii}| < 10^{-6}$ and the stream-wise mean stretch $|\langle \epsilon'_{11}(t) \rangle| < 10^{-4}$ is also close to zero. For all flows the distributions of both ϵ'_{ii} and ϵ'_{ij} for $j > i$, $i = 1 : 3$ are broad and exhibit a sharp cutoff due to the finite nature of Ω . In all cases, the standard deviation is large $\sigma_{\epsilon'_{ii}} \gg |\langle \epsilon'_{ii} \rangle|$, however the large number of independent observations (10^7) reduces the standard error to $\sigma_{\epsilon'_{ii}}/\sqrt{n} \sim 10^{-3}$, yielding accurate estimates of the principle stretches.

Figure 7(a,c) shows that the PDF of ϵ'_{11} is significantly broader for the isotropic case, which is attributed to confinement of streamlines to 2D streamsurfaces ψ_1, ψ_2 , leading to large velocity variations. The off-diagonal shears ϵ'_{ij} in Figure 7(b,d) are all similarly distributed except the longitudinal shears $\epsilon'_{12}, \epsilon'_{13}$ of the anisotropic flow are more broadly distributed as these streamlines are not confined to streamsurfaces and hence have higher curvature. The Protean transverse shear ϵ'_{23} in the isotropic case is zero as this is related to the helicity density as $\mathcal{H}(\mathbf{x}) = v'_i \varepsilon_{ijk} \epsilon'_{jk} = v \epsilon'_{23}$ (Lester *et al.* 2018a).

For isotropic flow, the Lyapunov exponent is effectively zero ($|\langle \epsilon'_{ii} \rangle| < 10^{-4}$), whereas for anisotropic flow it is slightly larger than the theoretical upper bound $\lambda_\infty = \ln 2$, ($\langle \epsilon'_{11} \rangle, \langle \epsilon'_{22} \rangle, \langle \epsilon'_{33} \rangle$) = (0.0001, 0.7148, -0.7149). The broad nature of the velocity gradient PDFs leads to a relatively large stretching variance, $\sigma_\lambda^2/\lambda_\infty \sim 10^2$ as shown in Figure 5d. This magnitude is consistent with the finding that the ensemble average (3.4) $h = \lambda_\infty + \sigma^2/2$ is not correct as this would not yield the agreement between h_{braid} and λ_∞ observed in Figure 6a. The broad distribution of all components of $\boldsymbol{\epsilon}'$ has significant impacts upon the range of fluid processes hosted in these flows, as shall be explored further in §5.2.

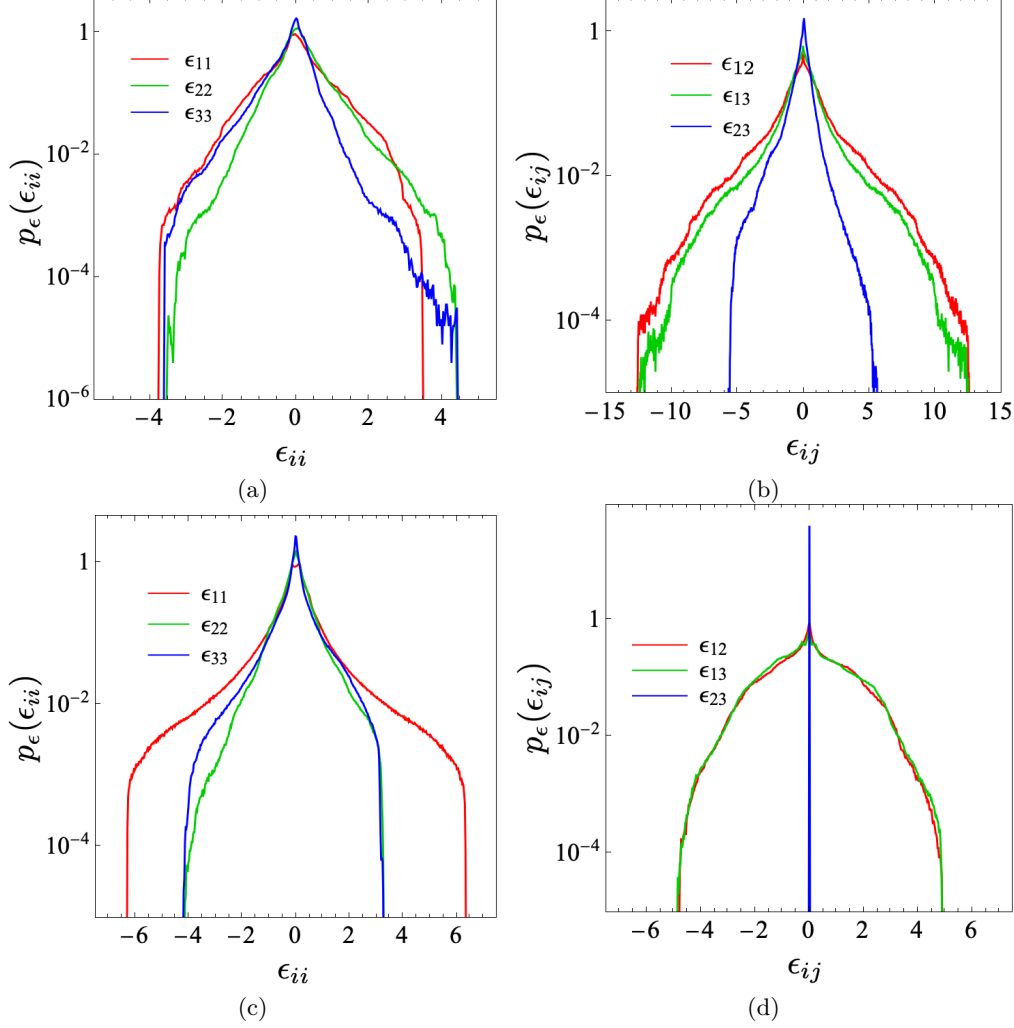


FIGURE 7. PDFs of (a,c) diagonal ϵ_{ii} and (b,d) off-diagonal velocity gradient components ϵ_{ij} for (top) heterogeneous anisotropic Darcy flow (4.1) with $\sigma_{\ln K}^2 = 4$, $\delta = 1$ and (bottom) isotropic Darcy flow (4.1) with $\sigma_{\ln K}^2 = 4$, $\delta = 0$.

5. Mechanisms and Implications of Chaotic Advection

5.1. Chaotic Advection Mechanisms

In this section we consider the mechanisms that generate chaotic advection in steady 3D Darcy flows ranging from flows with smooth, finite $\mathbf{K}(\mathbf{x})$ to those with impermeable inclusions or stagnation points. As $v_\phi \downarrow 0$, the rescaling (3.1) breaks down (Bajer 1994), leading to chaotic advection via a similar mechanism to that of pore-scale flow (Lester *et al.* 2013), where exponential stretching of fluid elements local to saddle-type stagnation points form stable and unstable hyperbolic manifolds and a heteroclinic tangle, the hallmark of chaos in continuous dynamical systems (Ottino 1989; Katok & Hasselblatt 1995). In the absence of stagnation points, chaotic advection via streamline braiding arises via a different mechanism that is most clearly elucidated by consideration of spatially periodic porous media. Consider Darcy flow in a heterogeneous anisotropic hydraulic conductivity field that is P -periodic in the direction of the mean potential

gradient $\mathbf{g} \equiv -\langle \nabla \phi \rangle / \|\langle \nabla \phi \rangle\|$,

$$\mathbf{K}(\mathbf{x}) = \mathbf{K}(\mathbf{x} + nP\mathbf{g}), \quad n = 1, 2, \dots \quad (5.1)$$

From the Brouwer fixed point theorem, there must exist period- k points \mathbf{x}_k (with $k = 1, 2, \dots$) in Ω , such that streamlines at \mathbf{x}_k are advected downstream to $\mathbf{x}_p + kP\mathbf{g}$.

Each periodic point \mathbf{x}_k belongs to a periodic orbit (streamline) that can generate chaotic advection in a similar manner to stagnation points in pore-scale flow. As per Hamiltonian dynamical systems theory (Katok & Hasselblatt 1995), a periodic point may be classified as a *hyperbolic saddle* point if the local fluid deformation over the k -period involves fluid stretching and contraction that is exponential in time, the directions of which are respectively associated with hyperbolic unstable and stable manifolds emanating from \mathbf{x}_k . If these manifolds intersect transversely (which is inevitable in random systems), then a heteroclinic tangle results, leading to chaotic advection (Ottino 1989; Katok & Hasselblatt 1995). For aperiodic braiding flows, hyperbolic un/stable manifolds arise via the same mechanisms but are not connected to features such as stagnation points or periodic orbits. Rather, they are detected by resolving hyperbolic Lagrangian coherent structures (Haller 2015) of the flow. The complex intermingling of these hyperbolic LCS generates the stretching and folding motions that are characteristic of chaotic advection. The random nature of heterogeneous Darcy flow means that non-hyperbolic LCSs such as KAM islands cannot occur, hence these flows are ergodic and hyperbolic.

5.2. Implications for Transport, Mixing and Reactions

The ubiquity of chaotic advection in heterogeneous Darcy flow has significant implications for the many fluidic processes hosted in this media, including transport and mixing of diffusive species such as solutes, colloids, reactive species and microorganisms. For these processes, the impact of chaotic dynamics scales with the Péclet number Pe as \sqrt{Pe} (Aref *et al.* 2017), which can be large as Pe ranges from 10^{-1} to 10^7 in Darcy flows (Delgado 2007; Bear 1972).

Chaotic advection leads to qualitative changes in solute mixing and transport. Le Borgne *et al.* (2013) use a lamellar mixing model (Duplat & Villiermaux 2008) to show that in non-chaotic steady 2D Darcy flow, the rate of mixing of diffusive solutes is governed by the rate of fluid deformation imparted by the medium heterogeneity. For 2D (Dentz *et al.* 2016) and 3D (Lester *et al.* 2021) isotropic Darcy flow, the rate of elongation $\rho(t) \equiv l(t)/l(0)$ of fluid elements grows algebraically as $\langle \rho(t) \rangle \sim t^r$, where the index $r = \mu + \nu$ varies from sublinear $r < 1$ to ballistic stretching $1 < r < 2$, depending upon the medium heterogeneity, and μ, ν respectively characterise the mean and variance of the fluid stretching process. The lamellar mixing model (Le Borgne *et al.* 2013) predicts that the concentration variance within the solute plume decays with time as

$$\langle c^2 \rangle \propto t^{-2\mu+2\nu+D_f+2}, \quad (5.2)$$

where D_f is the fractal dimension of material lines elongated by the flow. The lamellar mixing model also applies to turbulent and chaotic flows (Villiermaux & Duplat 2003; Meunier & Villiermaux 2010), yielding exponential decay of concentration variance as

$$\langle c^2 \rangle \propto \left(\frac{\lambda_\infty}{6t} \right)^{1/4} e^{-\lambda_\infty t/3}. \quad (5.3)$$

Hence mixing of diffusive solutes is rapidly accelerated by chaotic advection. Similarly, the peak concentration $c_m(t)$ of a Gaussian plume which is inversely proportional to the

dilution index $E(t) \equiv \exp[H(t)]$ (Kitanidis 1994) where $H(t)$ is the scalar entropy

$$H(t) = - \int_V d\mathbf{x} \frac{c(\mathbf{x}, t)}{\langle c \rangle} \ln \left[\frac{c(\mathbf{x}, t)}{\langle c \rangle} \right], \quad (5.4)$$

decays algebraically in non-chaotic heterogeneous porous media flow as (Dentz *et al.* 2018)

$$c_m(t) \propto \frac{1}{E(t)} \propto t^{-r}, \quad (5.5)$$

with $1 < r < 2$ (Dentz *et al.* 2016), whereas for chaotic flows these quantities evolve exponentially as

$$c_m(t) \propto \frac{1}{E(t)} \propto \exp(-\lambda_\infty t). \quad (5.6)$$

Hence chaotic advection accelerates the rate of solute mixing from algebraic to exponential.

Chaotic advection also significantly enhances transverse dispersion. In the purely advective limit $Pe \rightarrow \infty$, transverse dispersivity $D_{T,\infty}$ is zero in non-chaotic Darcy flow, whereas for chaotic flow $D_{T,\infty} \sim \lambda_\infty^2$ as per (3.9). For diffusive solutes, D_T in non-chaotic Darcy flow is proportional to molecular diffusivity D_m as (Lester *et al.* 2023)

$$D_T = D_m \langle m \rangle, \quad (5.7)$$

where m characterises fluctuations in streamlines due to heterogeneities in the conductivity field. A simple model of stretching-mediated dispersion around streamlines in chaotic Darcy flow that yields conservative dispersion estimates (see Appendix F for details) yields significantly larger transverse dispersivity than (5.7)

$$D_T = D_{T,\infty} + D_m \frac{\sinh(2\lambda_\infty t_d)}{2\lambda_\infty t_d}, \quad (5.8)$$

where t_d is the period of stretching events. Conversely, chaotic mixing suppresses longitudinal dispersion. Although results are not available for heterogeneous Darcy flow, studies of the impact of chaotic mixing on hold-up dispersion (Jones & Young 1994; Lester *et al.* 2018b) act as a guide for strongly heterogeneous media. For purely advective solutes, chaotic advection suppresses longitudinal variance from $\sigma_L^2(t) \sim t^2$ (Taylor 1953) for non-chaotic flows to $\sigma_L^2(t) \sim t^2/(\ln t)^3$ (Lester *et al.* 2010) due to increased sampling of advective velocities.

The impact of chaotic advection upon chemical reactions and biological activity is profound and multifaceted (Neufeld & Hernandez-Garcia 2009). For the simple case of fast binary reactions with Damkhöler number $Da \rightarrow \infty$, the effective reaction kinetics are governed by solute mixing (Valocchi *et al.* 2019; LeBorgne *et al.* 2014), hence the impacts outlined above for solute mixing directly translate to the rate and extent of these reactions. For simple binary reactions with finite Da , this acceleration becomes less pronounced with decreasing Da as the advective dynamics play less of a controlling role. Chaotic advection also has a profound impact upon more complex chemical, biological and geological reaction systems hosted in porous materials such as autocatalytic reactions, oscillatory reactions, bistable and competitive systems. Although these reaction systems converge toward a stable or stationary chemical state under well-mixed conditions, under incomplete mixing conditions often found in porous materials (Wright *et al.* 2017), transport of reactants can continually drive this system away from its local equilibrium (Neufeld & Hernandez-Garcia 2009). Hence the accelerated transport characteristics inherent to chaotic advection can fundamentally alter the dynamics of these

systems (Tél *et al.* 2005). Furthermore, the transport structures (LCSs) generated by these flows leading to qualitatively different macroscopic behaviour including, e.g., singularly enhanced reactions and altered stability of competitive species (Károlyi *et al.* 2000).

6. Conclusions

The prevalence of chaotic advection in heterogeneous Darcy flow is a key consideration as these kinematics profoundly impact the myriad fluid-borne processes in porous media, ranging from solute mixing and transport to colloidal transport, chemical reactions and biological activity (Aref *et al.* 2017). In this study we directly address the question of the existence of chaotic advection for steady 3D Darcy flow with smooth, finite hydraulic conductivity fields and find that chaotic advection is ubiquitous for all realistic models of heterogeneous porous media.

We establish that realistic models of Darcy scale heterogeneous porous media should possess anisotropic hydraulic conductivity tensor fields $\mathbf{K}(\mathbf{x})$. We rely on two results. First, experimental observations Bear (1972); Delgado (2007) show that transverse dispersion is ubiquitous in heterogeneous Darcy flow in the large Péclet number limit, i.e., purely advective conditions. Second, it has recently been proven Lester *et al.* (2023) that isotropic conductivity fields cannot admit purely advective transverse dispersion. Hence all realistic heterogeneous conductivity fields must also be anisotropic.

A recently uncovered quantitative relationship (3.9) (Lester *et al.* 2024) between the purely advective transverse dispersivity D_T and Lyapunov exponent λ_∞ in random unidirectional 3 dof flows also extends to steady 3D Darcy flow. This establishes that transverse dispersion and chaotic advection in steady 3D heterogeneous Darcy flow are intimately linked as both phenomena result from non-trivial streamline braiding, hence chaotic advection is inherent to these flows.

The onset of chaotic advection in steady 3D Darcy flow is considered via numerical simulations of flow in two classes of hydraulic conductivity fields; heterogeneous fields with variable anisotropy, and anisotropic fields with variable heterogeneity. We find that chaotic advection arises even for the weakest perturbations away from both isotropic heterogeneous media and anisotropic homogeneous media, establishing that chaotic advection is inherent to anisotropic heterogeneous media. Simple relationships are found for how D_T and λ_∞ scale with medium anisotropy parameter δ and conductivity log-variance $\sigma_{\ln K}^2$, and excellent agreement is found with the theoretical model (3.9) linking D_T and λ_∞ in randomly braiding 3 dof flows. In the limit of large $\sigma_{\ln K}^2$, the Lyapunov exponent of anisotropic media converges to $\lambda_\infty \approx 0.6772$, which is close to the theoretical upper bound $\lambda_{\infty, \max} = \ln 2 \approx 0.6931$ for 3 dof continuous systems, suggesting that highly heterogeneous Darcy flow is a strong mixing flow.

These results firmly establish the ubiquity of chaotic advection in steady 3D heterogeneous Darcy flow, and we show that these kinematics have profound implications for understanding, quantifying and predicting a wide range of processes at the Darcy scale. The main finding of this study points to several future research directions. Further investigation of the quantitative link (3.9) between D_T and λ_∞ is required, as D_T has been measured for a wide range of porous materials (Delgado 2007), whereas λ_∞ has only been measured in a small number of studies (Kree & Villiermaux 2017; Souzy *et al.* 2020; Heyman *et al.* 2020, 2021) at the pore scale. Development of methods to characterize chaotic mixing at the field scale are required, as well as investigation of the chaotic dynamics generated by geologically-relevant conductivity fields, and fields that generate anomalous transport. In the context of solute mixing and transport, further investigation

and quantitative prediction of concentration PDF, transverse and longitudinal dispersion of diffusive solutes is required. Furthermore, the impact of chaotic mixing upon chemical reactions and biological activity in Darcy flow is an open area.

The recognition that chaotic dynamics are inherent to porous media flow across all scales opens the door to the development of a broad class of upscaling methods that explicitly honour these kinematics. The ubiquity of macroscopic chaotic advection has profound implications for the myriad processes hosted in heterogeneous porous media, and calls for a fundamental re-evaluation of transport and reaction methods in macroscopic porous systems.

Appendix A. Proof of Zero Total Helicity H

We show that the total helicity H for conductivity fields of the form

$$\begin{aligned}\mathbf{K}(\mathbf{x}) &= \mathbf{K}_1(\mathbf{x}) + \mathbf{K}_2(\mathbf{x}), \\ &= k_0(\mathbf{x})\mathbf{I} + \delta k_0(\mathbf{x})\hat{\mathbf{e}}_1 \otimes \hat{\mathbf{e}}_1,\end{aligned}\tag{A 1}$$

are zero by expressing the corresponding velocity field as

$$\begin{aligned}\mathbf{v}(\mathbf{x}) &= -\mathbf{K}_1(\mathbf{x}) \cdot \nabla \phi - \mathbf{K}_2(\mathbf{x}) \cdot \nabla \phi, \\ &= \mathbf{v}_1(\mathbf{x}) + \mathbf{v}_2(\mathbf{x}),\end{aligned}\tag{A 2}$$

and thus the helicity density is

$$\begin{aligned}\mathcal{H}(\mathbf{x}) &= \mathbf{v}_1(\mathbf{x}) \cdot [\nabla \times \mathbf{v}_1(\mathbf{x})] + \mathbf{v}_2(\mathbf{x}) \cdot [\nabla \times \mathbf{v}_2(\mathbf{x})] \\ &\quad + \mathbf{v}_1(\mathbf{x}) \cdot [\nabla \times \mathbf{v}_2(\mathbf{x})] + \mathbf{v}_2(\mathbf{x}) \cdot [\nabla \times \mathbf{v}_1(\mathbf{x})],\end{aligned}\tag{A 3}$$

where the quantities on the top row of the RHS are zero. Expressing $\mathbf{v}_2(\mathbf{x}) = f(\mathbf{x})\hat{\mathbf{e}}_1$, then (A 3) simplifies to

$$\begin{aligned}\mathcal{H}(\mathbf{x}) &= f(\mathbf{x})\hat{\mathbf{e}}_1 \cdot [\nabla \times \mathbf{v}_1(\mathbf{x})] + \mathbf{v}_1(\mathbf{x}) \cdot [\nabla \times (f(\mathbf{x})\hat{\mathbf{e}}_1)] \\ &= \hat{\mathbf{e}}_1 \cdot (\nabla \times [f(\mathbf{x})\mathbf{v}_1(\mathbf{x})]) \\ &= \nabla \cdot (x_1 \nabla \times [f(\mathbf{x})\mathbf{v}_1(\mathbf{x})]).\end{aligned}\tag{A 4}$$

Hence the total helicity

$$H = \int_{\Omega} \mathcal{H}(\mathbf{x}) d\mathbf{x} = 0,\tag{A 5}$$

due to the divergence theorem and continuity of $f(\mathbf{x})$ and $\mathbf{v}_1(\mathbf{x})$ over the boundary $\partial\Omega$.

Appendix B. Fluid Deformation in Protean Coordinates

Fluid deformation is characterised by the deformation gradient tensor $\mathbf{F}(t; \mathbf{X})$ with Lagrangian coordinate \mathbf{X} , which evolves according to (3.10). The Lyapunov exponent and fluid stretching statistics are gathered by sampling ϵ along streamlines. The moving and rotating *Protean* coordinate frame provides several advantages as detailed in (Lester *et al.* 2018a) and briefly summarised as follows. The Protean coordinate frame \mathbf{x}' is related to the Eulerian frame \mathbf{x} as

$$\mathbf{x}'(t) = \mathbf{Q}(t) \cdot [\mathbf{x} - \mathbf{x}_0(t; \mathbf{X})],\tag{B 1}$$

where $\mathbf{x}_0(t; \mathbf{X})$ is the position of a fluid tracer particle at time t with initial position \mathbf{X} , and $\mathbf{Q}(t)$ is a time-dependent orthogonal rotation matrix. The Protean velocity gradient

tensor $\epsilon'(t; \mathbf{X})$ is related to the Lagrangian velocity gradient tensor $\epsilon(t)$ as

$$\epsilon'(t; \mathbf{X}) = \mathbf{Q}^\top(t) \cdot \epsilon(t; \mathbf{X}) \cdot \mathbf{Q}(t) + \dot{\mathbf{Q}}^\top(t) \cdot \mathbf{Q}(t), \quad (\text{B } 2)$$

The rotational matrix $\mathbf{Q}(t)$ aligns the x'_1 coordinate with the local velocity direction such that $\mathbf{e}'_1 = \mathbf{v}/v$, and for steady flow the Protean coordinate system is a streamline coordinate system. The rotation $\mathbf{Q}(t)$ is comprised of two subrotations as $\mathbf{Q}(t) = \mathbf{Q}_2(t) \cdot \mathbf{Q}_1(t)$, where the first rotation $\mathbf{Q}_1(t)$ aligns x'_1 with \mathbf{v}/v and so renders the ϵ'_{21} and ϵ'_{31} elements of the Protean velocity gradient tensor $\epsilon'(t; \mathbf{X})$ to be zero (Lester *et al.* 2018a). The second rotation $\mathbf{Q}_2(t)$ about the axis \mathbf{x}' in the streamwise direction is chosen such the remaining lower triangular element ϵ'_{23} is also zero (Lester *et al.* 2018a), rendering the Protean velocity gradient tensor upper triangular:

$$\epsilon' = \begin{pmatrix} \epsilon'_{11} & \epsilon'_{12} & \epsilon'_{13} \\ 0 & \epsilon'_{22} & \epsilon'_{23} \\ 0 & 0 & \epsilon'_{33} \end{pmatrix}. \quad (\text{B } 3)$$

Hence fluid deformation in the heterogeneous Darcy flows is characterised by computation of the Protean velocity gradient tensor along the streamlines of these flows.

Appendix C. Fluid Stretching in 3D Darcy Flow

The 1D CTRW (3.13) for evolution of $\rho(t; \mathbf{X})$ is derived by considering evolution of the infinitesimal line element $\delta \mathbf{l}(t; \mathbf{X}) = \mathbf{F}'(t; \mathbf{X}) \cdot \delta \mathbf{l}(0; \mathbf{X})$, the length of which evolves as

$$\delta l(t; \mathbf{X}) \equiv \|\delta \mathbf{l}(t; \mathbf{X})\| = \sqrt{\mathbf{l}(0; \mathbf{X}) \cdot \mathbf{C}(t; \mathbf{X}) \cdot \mathbf{l}(0; \mathbf{X})}, \quad (\text{C } 1)$$

where $\mathbf{C}(t; \mathbf{X}) = \mathbf{F}'(t; \mathbf{X})^\top \cdot \mathbf{F}'(t; \mathbf{X})$ is the symmetric Cauchy-Green tensor. Hence $\rho(t; \mathbf{X})$ grows with the largest eigenvalue $\nu(t; \mathbf{X})$ of $\mathbf{C}(t; \mathbf{X})$ as

$$\rho(t; \mathbf{X}) = \sqrt{\nu(t; \mathbf{X})}. \quad (\text{C } 2)$$

As detailed in Appendix B, the F'_{22} component characterises exponential stretching of fluid elements, and so converges to ρ (Lester *et al.* 2018a) in the asymptotic limit as

$$\lim_{t \rightarrow \infty} \frac{1}{t} \ln \rho(t; \mathbf{X}) = \lim_{t \rightarrow \infty} \frac{1}{2t} \ln \nu(t; \mathbf{X}) = \lim_{t \rightarrow \infty} \frac{1}{t} \ln F'_{22}(t; \mathbf{X}). \quad (\text{C } 3)$$

From (3.10), F'_{22} evolves with streamline distance s as

$$F'_{22,s}(s; \mathbf{X}) = \exp \left(\int_0^s \frac{\epsilon'_{22}(s'; \mathbf{X})}{v(s'; \mathbf{X})} ds' \right), \quad (\text{C } 4)$$

where $v(s; \mathbf{X}) = |\mathbf{v}(\mathbf{x}(s; \mathbf{X}))| = ds/dt$ is the local streamline velocity and $\mathbf{x}(s; \mathbf{X})$ is the position of a tracer particle along a streamline with initial position \mathbf{X} at $s = 0$, $t = 0$. As fluid velocity and velocity gradient are both spatially Markovian along streamlines (Le Borgne *et al.* 2008a; Lester *et al.* 2022), s may be discretized with respect to the spatial velocity correlation length ℓ as $s_n = n\ell$, with $n = 0, 1, \dots$, as per (3.13). Similarly, the advection time t_n and length stretch $\rho_n \equiv F'_{22,s}(s_n; \mathbf{X})$ at position s_n along a streamline evolves as per (3.13), with $v_n \equiv v(s_n; \mathbf{X})$, $\epsilon_n \equiv \epsilon'_{22}(s_n; \mathbf{X})$. Thus the CTRW (3.13) captures the line stretching dynamics in steady heterogeneous 3D Darcy flow.

C.1. Fluid Stretching Under Normal Transport

Following (Dentz *et al.* 2016), from the CTRW (3.13), the Fourier-Laplace transform $\hat{p}_{\zeta,t}(k, \lambda)$ of the PDF $p_{\zeta,t}(\zeta, t)$ where λ is the Laplace variable for ζ and k is the Fourier

variable for t is given by

$$\hat{p}_{\zeta,t}(k, \lambda) = \frac{1 - \psi(\lambda)}{\lambda} \frac{1}{1 - \psi(k, \lambda)}, \quad (\text{C } 5)$$

where $\psi(k, \lambda)$ is given by

$$\psi(k, \lambda) = \psi(\lambda) + \int_0^\infty dt \exp(-\lambda t) [\cos(|k|\epsilon t) - 1] \psi(t), \quad (\text{C } 6)$$

and $\psi(\lambda)$ is the Laplace transform of $\psi(\tau)$. The moments of ζ are defined in terms of $\hat{p}_{\zeta,t}(k, \lambda)$ by

$$m_{j,\zeta} = (-i)^j \frac{\partial^j \hat{p}_{\zeta,t}(k, \lambda)}{\partial k^j} \Big|_{k=0}. \quad (\text{C } 7)$$

Hence

$$m_{1,\zeta} = 0, \quad m_{2,\zeta} = -\frac{1}{\lambda[1 - \psi(\lambda)]} \frac{\partial^2 \psi(k, \lambda)}{\partial k^2} \Big|_{k=0}, \quad (\text{C } 8)$$

and the small k -expansion of (C 6) is

$$\psi(k, \lambda) = \psi(\lambda) - \int_0^\infty dt \exp(-\lambda t) \frac{1}{2} k^2 \sigma_\epsilon^2 t^2 \psi(t) + \dots \quad (\text{C } 9)$$

and additional small λ -expansion

$$\psi(k, \lambda) = 1 - k^2 \sigma_\epsilon^2 \langle \tau^2 \rangle + \dots \quad (\text{C } 10)$$

The small λ -expansion of $\psi(\lambda)$ is

$$\psi(\lambda) = 1 - \langle \tau \rangle \lambda + \frac{1}{2} \langle \tau^2 \rangle \lambda^2, \quad (\text{C } 11)$$

thus, we obtain to leading order

$$m_{2,\zeta} = \frac{\sigma_\epsilon^2 \langle \tau^2 \rangle}{\lambda^2 \langle \tau \rangle}, \quad (\text{C } 12)$$

the inverse Laplace transform of which gives

$$\lim_{t \rightarrow \infty} \sigma_{\ln \rho}^2 = \sigma_\epsilon^2 \frac{\langle \tau^2 \rangle}{\langle \tau \rangle} t \equiv \sigma_\lambda^2 t. \quad (\text{C } 13)$$

Appendix D. Numerical Solvers and Streamline Tracking

The potential fluctuation equation (4.4) for Darcy flow is solved to precision 10^{-16} on a uniform structured 256^3 grid using a high resolution eighth-order compact finite difference scheme (Lele 1992). To generate high resolution results and preserve the Lagrangian kinematics of the flow, we use a similar numerical approach to that used in (Lester *et al.* 2019). Specifically, we perform a triply-periodic 5-th order spline interpolation of the primitive variables $\phi(\mathbf{x})$, $\mathbf{K}(\mathbf{x})$ from their grid values and reconstruct the potential field $\phi(\mathbf{x})$ according to (4.3). The velocity field is then computed analytically from these fields as $\mathbf{v}(\mathbf{x}) = -\mathbf{K}(\mathbf{x}) \cdot \nabla \phi(\mathbf{x})$, ensuring that the velocity field is triply-periodic and C_4 continuous and the velocity gradient is accurately resolved for computation of fluid deformation in the Protean frame. This approach also implicitly enforces the helicity-free

constraint $h(\mathbf{x}) = 0$ for the case of isotropic conductivity tensor $\mathbf{K}(\mathbf{x}) = k(\mathbf{x})\mathbf{I}$ for $\delta = 0$. For the 256^3 mesh the local relative divergence error

$$d(\mathbf{x}) = \frac{|\nabla \cdot \mathbf{v}(\mathbf{x})|}{\|\nabla \mathbf{v}(\mathbf{x})\|}, \quad (\text{D } 1)$$

of the interpolated velocity field $\mathbf{v}(\mathbf{x})$ is order 10^{-4} and the velocity gradient is accurate to order 10^{-3} .

Streamline tracking is then computed by solving the advection equation from the initial Lagrangian coordinate \mathbf{X} as

$$\frac{d\mathbf{x}}{dt} = \mathbf{v}(\mathbf{x}(t; \mathbf{X})), \quad \mathbf{x}(0; \mathbf{X}) = \mathbf{X}, \quad (\text{D } 2)$$

via a 5-th order Cash-Karp Runge-Kutta scheme to precision 10^{-14} . The periodic boundaries allow advection of fluid streamlines over many multiples of the solution domain Ω , facilitating study of the Lagrangian kinematics over arbitrary distances. Although the corresponding velocity field is periodic in space, when the flow is chaotic the streamlines are aperiodic and eventually sample all of the conductivity field in an ergodic manner.

While accurate, this streamline tracking method (along with all numerical schemes which do not explicitly enforce kinematic constraints) has been shown (Lester *et al.* 2023) to introduce spurious transverse dispersion for the isotropic zero helicity density flow $h = 0$ due to numerical streamlines not following their analytic counterparts. To circumvent this problem for the helicity-free case $\delta = 0$, we instead solve the invariant streamfunctions $\psi_1(\mathbf{x})$, $\psi_2(\mathbf{x})$ for the velocity field $\mathbf{v}(\mathbf{x}) = \nabla\psi_1(\mathbf{x}) \times \nabla\psi_2(\mathbf{x})$ via the following governing equations (Lester *et al.* 2022) to precision 10^{-16} using the same finite-difference method as described above:

$$\nabla^2\psi_1(\mathbf{x}) - \nabla f(\mathbf{x}) \cdot \nabla\psi_1(\mathbf{x}) = S_1(\psi_1, \psi_2), \quad (\text{D } 3)$$

$$\nabla^2\psi_2(\mathbf{x}) - \nabla f(\mathbf{x}) \cdot \nabla\psi_2(\mathbf{x}) = S_2(\psi_1, \psi_2), \quad (\text{D } 4)$$

where $f = \ln k$ and

$$S_1 = \frac{(\mathbf{B} \times \psi_2) \cdot (\nabla\psi_1 \times \nabla\psi_2)}{|\nabla\psi_1 \times \nabla\psi_2|} \quad S_2 = \frac{(\mathbf{B} \times \psi_1) \cdot (\nabla\psi_1 \times \nabla\psi_2)}{|\nabla\psi_1 \times \nabla\psi_2|}, \quad (\text{D } 5)$$

and

$$\mathbf{B} \equiv (\nabla\psi_1 \cdot \nabla)\nabla\psi_2 - (\nabla\psi_2 \cdot \nabla)\nabla\psi_1. \quad (\text{D } 6)$$

Similar to the Darcy equation, continuous streamfunctions $\psi_1(\mathbf{x})$, $\psi_2(\mathbf{x})$ are reconstructed from grid data using triply-periodic splines and the velocity field is computed analytically from these streamfunctions. As shown in (Lester *et al.* 2022), this method yields the same velocity field (to within numerical error) as that given by direct solution of the Darcy equation.

Each family of streamfunctions ψ_i is comprised of a *foliation* of non-intersecting stream-surfaces $\psi_i = \text{const.}$ that span the flow domain and constrain the Lagrangian kinematics of the flow. This flow structure is non-chaotic as the advection equation (D 2) simplifies to

$$\frac{ds}{dt} = v(s; \psi_1(\mathbf{X}), \psi_2(\mathbf{X})), \quad s(t = 0; \mathbf{X}) = 0, \quad (\text{D } 7)$$

where s is the distance travelled along a streamline of a tracer particle with initial position \mathbf{X} . The velocity magnitude $v(s; \psi_1(\mathbf{X}), \psi_2(\mathbf{X}))$ at the intersection of the streamsurfaces

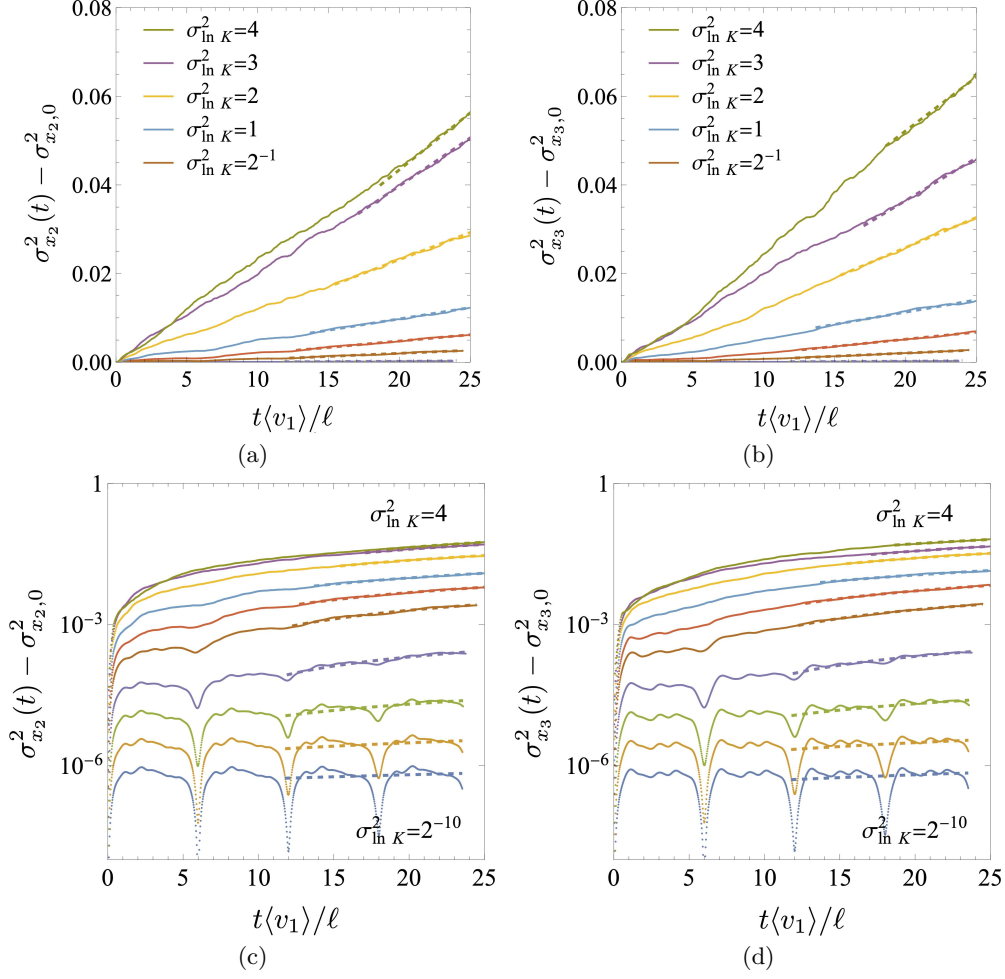


FIGURE 8. Evolution of transverse scalar variances $\sigma_{x_2}^2(t)$ (left), $\sigma_{x_3}^2(t)$ (right) with dimensionless travel time $t\langle v_1 \rangle / \ell$ in linear (top) and logarithmic (bottom) scales for heterogeneous anisotropic Darcy flow for various values of log-variance $\sigma_{\ln K}^2$. Fitted linear trend (dashed lines) at late times is used to estimate transverse dispersivities D_{22} , D_{33} .

$\psi_1(\mathbf{x}) = \psi_1(\mathbf{X})$, $\psi_2(\mathbf{x}) = \psi_2(\mathbf{X})$ only varies with s . Equation (D 7) is *integrable* in that ψ_1 , ψ_2 represent two invariants of the flow in the 3D domain, resulting in only one degree of freedom (distance) for streamlines of the flow to explore. For helicity-free flow, we perform streamline tracking via numerical integration of (D 7) to precision 10^{-8} . This approach ensures numerical streamlines follow their analytic counterparts and so enforces zero transverse dispersion and prevents the non-trivial braiding of streamlines that lead to chaotic advection.

Appendix E. Calculation of Transverse Dispersivity

For both the variable anisotropy and variable heterogeneity Darcy flows, transverse dispersivity is determined by tracking $N_p = 10^3$ streamlines over 10^3 traverses of the periodic domain Ω seeded from random locations within Ω . From these streamlines, the

transverse variances are computed as

$$\sigma_{x_2}^2(t) = \frac{1}{N_p} \sum_{i=1}^{N_p} (x_{2,i}(t) - \langle x_2 \rangle(t))^2, \quad \langle x_2 \rangle(t) = \frac{1}{N_p} \sum_{i=1}^{N_p} x_{2,i}(t), \quad (\text{E } 1)$$

$$\sigma_{x_3}^2(t) = \frac{1}{N_p} \sum_{i=1}^{N_p} (x_{3,i}(t) - \langle x_3 \rangle(t))^2, \quad \langle x_3 \rangle(t) = \frac{1}{N_p} \sum_{i=1}^{N_p} x_{3,i}(t). \quad (\text{E } 2)$$

For the anisotropic Darcy flow with variable heterogeneity, the transverse variances exhibit slow growth and periodic oscillations in Figure 8 for weak conductivity variance $\sigma_{\ln K}^2 \ll 1$ as the streamlines of the flow are nearly periodic. With increasing heterogeneity $\sigma_{\ln K}^2$, these orbits lose periodicity and ergodically explore the flow domain, resulting in stronger growth of the transverse variances. The transverse dispersivities are related to the asymptotic variance growth as

$$D_{22} = \frac{1}{2} \lim_{t \rightarrow \infty} \frac{d\sigma_{x_2}^2}{dt} \quad D_{33} = \frac{1}{2} \lim_{t \rightarrow \infty} \frac{d\sigma_{x_3}^2}{dt}. \quad (\text{E } 3)$$

To estimate this asymptotic growth we fit a linear function to the asymptotic variance data over two periods of the flow, as shown in Figure 8. Note that the variance data in Figure 8 has been truncated to 20 correlation lengths for illustrative purposes. The total transverse dispersivity D_T is then computed as the average of the x_2 x_3 dispersivities.

Appendix F. Estimate of Diffusive Transverse Dispersivity

To generate a conservative estimate of diffusive transverse dispersivity D_T under the action of chaotic advection, we consider a simple model for fluid deformation around a streamline at Lagrangian position \mathbf{X}_0 oriented in the $\mathbf{v}/v = \hat{\mathbf{e}}'_1$ direction of the Protean frame. Evolution of the local fluid deformation gradient tensor along the streamline is modeled via a “stretch and relax” process over period t_d as

$$\mathbf{F}_0(t) = \begin{cases} \mathbf{F}_{00}(t) & \text{for } 0 < t \leq t_d, \\ \mathbf{F}_{00}(t_d - t) & \text{for } t_d < t \leq 2t_d, \end{cases} \quad (\text{F } 1)$$

and $\mathbf{F}_{00}(t) = \exp(\lambda_\infty t) \hat{\mathbf{e}}'_2 \otimes \hat{\mathbf{e}}'_2 + \exp(-\lambda_\infty t) \hat{\mathbf{e}}'_3 \otimes \hat{\mathbf{e}}'_3$ characterizes the transverse stretching and contraction process. The deformation gradient tensor $\mathbf{F}(\mathbf{X}_0, t)$ on a streamline with Lagrangian coordinate \mathbf{X}_0 is then modelled as a series of sequential “stretch and relax” processes with uniformly distributed random orientation $\theta \in [0, 2\pi]$ as

$$\mathbf{F}(\mathbf{X}, t) = [\mathbf{R}(\theta_n) \cdot \mathbf{F}_0(t) \cdot \mathbf{R}(\theta_n)^\top] \cdot \dots \cdot [\mathbf{R}(\theta_1) \cdot \mathbf{F}_0(2t_d) \cdot \mathbf{R}(\theta_1)^\top], \quad (\text{F } 2)$$

where $\mathbf{R}(\theta)$ is the rotation matrix around $\hat{\mathbf{e}}'_1$ and $n = \lceil t/(2t_d) \rceil$. This simple model generates a conservative estimate of dispersion as it does not capture persistent exponential stretching of fluid elements. However, such stretching in the absence of folding leads to erroneous predictions of transverse dispersion that grow exponentially in time. In practice, folding suppresses transverse dispersion to be sub-exponential, however incorporation of such second-order deformation measures is beyond the scope of this model.

A solute packet centered about a streamline with Eulerian coordinate $\mathbf{x}_0(t) \equiv \mathbf{x}(\mathbf{X}_0, t)$ with initial concentration $c(\mathbf{x}, 0) = \delta(\mathbf{x} - \mathbf{x}_0)$ evolves with a Gaussian concentration profile

$$c(\mathbf{x}, t) = \frac{1}{\sqrt{(2\pi)^d \det \boldsymbol{\Sigma}(t)}} \exp \left(-\frac{1}{2} (\mathbf{x} - \mathbf{x}_0(t)) \cdot \boldsymbol{\Sigma}^{-1}(t) \cdot (\mathbf{x} - \mathbf{x}_0(t)) \right), \quad (\text{F } 3)$$

where the covariance matrix $\Sigma(t)$ evolves as (Dentz *et al.* 2018)

$$\Sigma(t) = 2D_m \mathbf{F}'(\mathbf{X}_0, t) \cdot \left(\int_0^t \mathbf{F}'(\mathbf{X}_0, t')^{-1} \cdot \mathbf{F}'(\mathbf{X}_0, t')^{-\top} dt' \right) \cdot \mathbf{F}'(\mathbf{X}_0, t)^\top, \quad (\text{F } 4)$$

which from (F 2) simplifies to

$$\Sigma(2nt_d) = 2D_m \sum_{i=1}^n \mathbf{R}(\theta_n) \cdot \mathbf{\Lambda}_0 \cdot \mathbf{R}(\theta_n)^\top, \quad (\text{F } 5)$$

where

$$\mathbf{\Lambda}_0 = \frac{1 - e^{-2\hat{\lambda}_\infty t_d}}{\hat{\lambda}_\infty} \hat{\mathbf{e}}'_2 \otimes \hat{\mathbf{e}}'_2 + \frac{e^{2\hat{\lambda}_\infty t_d} - 1}{\hat{\lambda}_\infty} \hat{\mathbf{e}}'_2 \otimes \hat{\mathbf{e}}'_2. \quad (\text{F } 6)$$

Hence for large t , the covariance matrix converges to $\Sigma(t) = 2D_m n \langle \mathbf{\Lambda} \rangle$ where

$$\langle \mathbf{\Lambda} \rangle \equiv \frac{1}{2\pi} \int_0^{2\pi} [\mathbf{R}(\theta) \cdot \mathbf{\Lambda}_0 \cdot \mathbf{R}(\theta)^\top] d\theta \quad (\text{F } 7)$$

and so

$$\Sigma(t) = 2D_m t \frac{\sinh 2\hat{\lambda}_\infty t_d}{2\hat{\lambda}_\infty t_d} \mathbf{1}. \quad (\text{F } 8)$$

Hence transverse dispersion around streamlines is exponentially amplified by periodic stretching. In conjunction with advective dispersion of streamlines, this yields (5.8). Note that similar to (5.7), this model is only valid for $\|\Sigma(t)\| < \ell$.

REFERENCES

- ALONSO-MATILLA, ROBERTO, CHAKRABARTI, BRATO & SAINTILLAN, DAVID 2019 Transport and dispersion of active particles in periodic porous media. *Physical Review Fluids* **4** (4), 043101.
- DE ANNA, PIETRO, JIMENEZ-MARTINEZ, JOAQUIN, TABUTEAU, HERVÉ, TURUBAN, REGIS, LE BORGNE, TANGUY, DERRIEN, MORGANE & MÉHEUST, YVES 2013 Mixing and reaction kinetics in porous media: an experimental pore scale quantification. *Environ. Sci. Technol.* **48** (1), 508–516.
- AREF, H. 1984 Stirring by chaotic advection. *Journal of Fluid Mechanics* **143**, 1–21.
- AREF, HASSAN, BLAKE, JOHN R, BUDIŠIĆ, MARKO, CARDOSO, SILVANA SS, CARTWRIGHT, JULYAN HE, CLERCX, HERMAN JH, EL OMARI, KAMAL, FEUDEL, ULRIKE, GOLESTANIAN, RAMIN, GOUILLART, EMMANUELLE *et al.* 2017 Frontiers of chaotic advection. *Reviews of Modern Physics* **89** (2), 025007.
- ARNOL'D, V. I. 1965 Sur la topologie des écoulements stationnaires des fluides parfaits. *Comptes Rendus Acad. Sci. Paris* **261**, 312–314.
- ARTIN, EMIL 1947 Theory of braids. *Annals of Mathematics* **48**, 101–126.
- BAJER, K. 1994 Hamiltonian formulation of the equations of streamlines in three-dimensional steady flows. *Chaos, Solitons and Fractals* **4** (6), 895–911.
- BEAR, J. 1972 *Dynamics of Fluids in Porous Media*. *Dover Classics of Science and Mathematics* 1. Dover.
- BEAUDOIN, A. & DE DREUZY, J.-R. 2013 Numerical assessment of 3-d macrodispersion in heterogeneous porous media. *Water Resources Research* **49** (5), 2489–2496.
- BERKOWITZ, BRIAN, CORTIS, ANDREA, DENTZ, MARCO & SCHER, HARVEY 2006 Modeling non-fickian transport in geological formations as a continuous time random walk. *Reviews of Geophysics* **44** (2).
- BOON, MAARTJE, BIJELJIC, BRANKO, NIU, BEN & KREVER, SAM 2016 Observations of 3-D transverse dispersion and dilution in natural consolidated rock by x-ray tomography. *Adv. Water Resour.* **96**, 266 – 281.

- BOYLAND, PHILIP L., AREF, HASSAN & STREMLER, MARK A. 2000 Topological fluid mechanics of stirring. *Journal of Fluid Mechanics* **403**, 277–304.
- BRENNER, H. & EDWARDS, D. 1993 *Macrotransport Processes*. Butterworth-Heinemann, MA, USA.
- CATALAN, THIAGO 2019 A link between topological entropy and lyapunov exponents. *Ergodic Theory and Dynamical Systems* **39** (3), 620–637.
- CERBELLI, STEFANO, GIONA, MASSIMILIANO, GORODETSKYI, OLEXANDER & ANDERSON, PATRICK D. 2017 Singular eigenvalue limit of advection-diffusion operators and properties of the strange eigenfunctions in globally chaotic flows. *The European Physical Journal Special Topics* **226** (10), 2247–2262.
- CHAUDHURI, A. & SEKCHAR, M. 2005 Analytical solutions for macrodispersion in a 3d heterogeneous porous medium with random hydraulic conductivity and dispersivity. *Transport in Porous Media* **58** (3), 217–241.
- CHIOGNA, GABRIELE, ROLLE, MASSIMO, BELLIN, ALBERTO & CIRPKA, OLAF A. 2014 Helicity and flow topology in three-dimensional anisotropic porous media. *Advances in Water Resources* **73**, 134–143.
- CHO, MICHELLE S., SOLANO, FELIPE, THOMSON, NEIL R., TREFRY, MICHAEL G., LESTER, DANIEL R. & METCALFE, GUY 2019 Field trials of chaotic advection to enhance reagent delivery. *Groundwater Monitoring & Remediation* **39** (3), 23–39.
- CIRPKA, OLAF A., CHIOGNA, GABRIELE, ROLLE, MASSIMO & BELLIN, ALBERTO 2015 Transverse mixing in three-dimensional nonstationary anisotropic heterogeneous porous media. *Water Resources Research* **51** (1), 241–260.
- COCKE, W. J. 1969 Turbulent hydrodynamic line stretching: Consequences of isotropy. *The Physics of Fluids* **12** (12), 2488–2492.
- CUSHMAN, JOHN H 2013 *The physics of fluids in hierarchical porous media: Angstroms to miles*, vol. 10. Springer Science & Business Media.
- DAGAN, G. 1989 *Flow and transport in porous formations*. Springer, New York.
- DARTOIS, ARTHUR, BEAUDOIN, ANTHONY & HUBERSON, SERGE 2018 Impact of local diffusion on macroscopic dispersion in three-dimensional porous media. *Comptes Rendus Mécanique* **346** (2), 89–97.
- DELGADO, JMPQ 2007 Longitudinal and transverse dispersion in porous media. *Chemical Engineering Research and Design* **85** (9), 1245–1252.
- DENTZ, M., DE BARROS, F. P. J., LE BORGNE, T. & LESTER, D. R. 2018 Evolution of solute blobs in heterogeneous porous media. *Journal of Fluid Mechanics* **853**, 621–646.
- DENTZ, MARCO, CREPPY, ADAMA, DOUARCHE, CARINE, CLÉMENT, ERIC & AURADOU, HAROLD 2022 Dispersion of motile bacteria in a porous medium. *Journal of Fluid Mechanics* **946**, A33.
- DENTZ, MARCO, HIDALGO, JUAN J. & LESTER, DANIEL 2023 Mixing in porous media: Concepts and approaches across scales. *Transport in Porous Media* **146** (1), 5–53.
- DENTZ, MARCO, LE BORGNE, TANGUY, LESTER, DANIEL R. & DE BARROS, FELIPE P. J. 2015 Scaling forms of particle densities for lévy walks and strong anomalous diffusion. *Phys. Rev. E* **92**, 032128.
- DENTZ, MARCO, LESTER, DANIEL R., LE BORGNE, TANGUY & DE BARROS, FELIPE P. J. 2016 Coupled continuous-time random walks for fluid stretching in two-dimensional heterogeneous media. *Phys. Rev. E* **94**, 061102.
- DINH, TIEN-CUONG & SIBONY, NESSIM 2008 Upper bound for the topological entropy of a meromorphic correspondence. *Israel Journal of Mathematics* **163** (1), 29–44.
- DUPLAT, J., INNOCENTI, C. & VILLERMAUX, E. 2010 A nonsequential turbulent mixing process. *Phys. Fluids* **22** (3), 035104.
- DUPLAT, J. & VILLERMAUX, E. 2008 Mixing by random stirring in confined mixtures. *J. Fluid Mech.* **617**, 51–86.
- FEREDAY, D. R. & HAYNES, P. H. 2004 Scalar decay in two-dimensional chaotic advection and batchelor-regime turbulence. *Physics of Fluids* **16** (12), 4359–4370.
- GELHAR, LYNN W. & AXNESS, CARL L. 1983 Three-dimensional stochastic analysis of macrodispersion in aquifers. *Water Resources Research* **19** (1), 161–180.
- GIRIMAJI, S. S. & POPE, S. B. 1990 Material-element deformation in isotropic turbulence. *Journal of Fluid Mechanics* **220**, 427–458.

- HACKERT, C. L., ELLZEY, J. L., EZEKOYE, O. A. & HALL, M. J. 1996 Transverse dispersion at high peclet numbers in short porous media. *Experiments in Fluids* **21** (4), 286–290.
- HAKOUN, VIVIEN, COMOLLI, ALESSANDRO & DENTZ, MARCO 2019 Upscaling and prediction of lagrangian velocity dynamics in heterogeneous porous media. *Water Resources Research* **55** (5), 3976–3996.
- HALL, TOBY & YURTTAŞ, S. ÖYKÜ 2009 On the topological entropy of families of braids. *Topology and its Applications* **156** (8), 1554–1564.
- HALLER, GEORGE 2015 Lagrangian coherent structures. *Annual Review of Fluid Mechanics* **47** (Volume 47, 2015), 137–162.
- HALLER, GEORGE & SAPSIS, THEMISTOKLIS 2008 Where do inertial particles go in fluid flows? *Physica D: Nonlinear Phenomena* **237** (5), 573 – 583.
- HANDEL, MICHAEL & THURSTON, WILLIAM P 1985 New proofs of some results of nielsen. *Advances in Mathematics* **56** (2), 173–191.
- HEYMAN, J., LESTER, D. R. & LE BORGNE, T. 2021 Scalar signatures of chaotic mixing in porous media. *Phys. Rev. Lett.* **126**, 034505.
- HEYMAN, JORIS, LESTER, DANIEL R., TURUBAN, RÉGIS, MÉHEUST, YVES & LE BORGNE, TANGUY 2020 Stretching and folding sustain microscale chemical gradients in porous media. *Proceedings of the National Academy of Sciences* **117** (24), 13359–13365.
- HINCH, E. J. 1999 *Mixing: Turbulence and Chaos — An Introduction*, pp. 37–56. Boston, MA: Springer US.
- HOLM, DARRYL D. & KIMURA, YOSHIFUMI 1991 Zero-helicity Lagrangian kinematics of three-dimensional advection. *Physics of Fluids A: Fluid Dynamics* **3** (5), 1033–1038.
- JANKOVIĆ, IGOR, STEWARD, DAVID R., BARNES, RANDAL J. & DAGAN, GEDEON 2009 Is transverse macrodispersivity in three-dimensional groundwater transport equal to zero? a counterexample. *Water Resources Research* **45** (8).
- JONES, S. W. & YOUNG, W. R. 1994 Shear dispersion and anomalous diffusion by chaotic advection. *Journal of Fluid Mechanics* **280**, 149–172.
- KALDA, JAAN 2000 Simple model of intermittent passive scalar turbulence. *Phys. Rev. Lett.* **84**, 471–474.
- KÁROLYI, GYÖRGY, PÉNTÉK, ÁRON, SCHEURING, ISTVÁN, TÉL, TAMÁS & TOROCZKAI, ZOLTÁN 2000 Chaotic flow: The physics of species coexistence. *Proceedings of the National Academy of Sciences* **97** (25), 13661–13665.
- KATOK, ANATOLE & HASSELBLATT, BORIS 1995 *Introduction to the Modern Theory of Dynamical Systems. Encyclopedia of Mathematics and its Applications* 1. Cambridge University Press.
- KITANIDIS, PETER K. 1994 The concept of the dilution index. *Water Resources Research* **30**, 2011–2026.
- KREE, MIHKEL & VILLERMAUX, EMMANUEL 2017 Scalar mixtures in porous media. *Phys. Rev. Fluids* **2**, 104502.
- LE BORGNE, TANGUY, DENTZ, MARCO & CARRERA, JESUS 2008a Lagrangian statistical model for transport in highly heterogeneous velocity fields. *Phys. Rev. Lett.* **101**, 090601.
- LE BORGNE, TANGUY, DENTZ, MARCO & CARRERA, JESUS 2008b Spatial markov processes for modeling lagrangian particle dynamics in heterogeneous porous media. *Phys. Rev. E* **78**, 026308.
- LE BORGNE, TANGUY, DENTZ, MARCO & VILLERMAUX, EMMANUEL 2013 Stretching, coalescence, and mixing in porous media. *Phys. Rev. Lett.* **110**, 204501.
- LE BORGNE, T., DENTZ, M. & VILLERMAUX, E. 2015 The lamellar description of mixing in porous media. *Journal of Fluid Mechanics* **770**, 458–498.
- LEBORGNE, TANGUY, GINN, TIMOTHY R. & DENTZ, MARCO 2014 Impact of fluid deformation on mixing-induced chemical reactions in heterogeneous flows. *Geophysical Research Letters* **41** (22), 7898–7906.
- LELE, SANJIVA K. 1992 Compact finite difference schemes with spectral-like resolution. *Journal of Computational Physics* **103**, 16–42.
- LESTER, D.R., TREFRY, M.G. & METCALFE, G. 2016 Chaotic advection at the pore scale: Mechanisms, upscaling and implications for macroscopic transport. *Advances in Water Resources* **97**, 175 – 192.
- LESTER, DANIEL R., BANDOPADHYAY, ADITYA, DENTZ, MARCO & LE BORGNE, TANGUY 2019

- Hydrodynamic dispersion and lamb surfaces in darcy flow. *Transport in Porous Media* **130** (3), 903–922.
- LESTER, DANIEL R. & DENTZ, MARCO 2024 Equating topological entropy and lyapunov exponent in ergodic flows. *Physical Review Fluids* (submitted).
- LESTER, DANIEL R., DENTZ, MARCO, BANDOPADHYAY, ADITYA & BORGNE, TANGUY LE 2022 Fluid deformation in isotropic Darcy flow. *Journal of Fluid Mechanics* **945**, A18.
- LESTER, DANIEL R., DENTZ, MARCO, BANDOPADHYAY, ADITYA & LE BORGNE, TANGUY 2021 The Lagrangian kinematics of three-dimensional Darcy flow. *Journal of Fluid Mechanics* **918**, A27.
- LESTER, D. R., DENTZ, M., BORGNE, T. LE & BARROS, F. P. J. DE 2018*a* Fluid deformation in random steady three-dimensional flow. *Journal of Fluid Mechanics* **855**, 770–803.
- LESTER, DANIEL R., DENTZ, MARCO, SINGH, PRAJWAL & BANDOPADHYAY, ADITYA 2023 Under what conditions does transverse macrodispersion exist in groundwater flow? *Water Resources Research* **59** (3), e2022WR033059.
- LESTER, DANIEL R., KUAN, BENNY & METCALFE, GUY 2018*b* Simultaneous optimisation of residence time, heat and mass transfer in laminar duct flows. *Chemical Engineering Science* **191**, 511–524.
- LESTER, D. R., METCALFE, G. & TREFRY, M. G. 2013 Is chaotic advection inherent to porous media flow? *Phys. Rev. Lett.* **111**, 174101.
- LESTER, D. R., METCALFE, G. & TREFRY, M. G. 2014 Anomalous transport and chaotic advection in homogeneous porous media. *Phys. Rev. E* **90**, 063012.
- LESTER, DANIEL R., METCALFE, GUY & TREFRY, MICHAEL G. 2024 Linking disperison and braiding in randomly stirred flows. *Physical Review Fluids* .
- LESTER, D. R., RUDMAN, M., METCALFE, G., TREFRY, M. G., ORD, A. & HOBBS, B. 2010 Scalar dispersion in a periodically reoriented potential flow: Acceleration via Lagrangian chaos. *Phys. Rev. E* **81**, 046319.
- MATSUOKA, CHIHIRO & HIRAIDE, KOICHI 2015 Computation of entropy and Lyapunov exponent by a shift transform. *Chaos: An Interdisciplinary Journal of Nonlinear Science* **25** (10), 103110.
- MAYS, DAVID C. & NEUPAUER, ROSEANNA M. 2012 Plume spreading in groundwater by stretching and folding. *Water Resources Research* **48** (7).
- METCALFE, GUY, LESTER, DANIEL, ORD, ALISON, KULKARNI, PANDURANG, TREFRY, MIKE, HOBBS, BRUCE E., REGENAUR-LIEB, KLAUS & MORRIS, JEFFERY 2010 A partially open porous media flow with chaotic advection: towards a model of coupled fields. *Philosophical Transactions of the Royal Society A: Mathematical, Physical and Engineering Sciences* **368** (1910), 217–230.
- METCALFE, GUY, LESTER, DANIEL & TREFRY, MICHAEL 2023 A primer on the dynamical systems approach to transport in porous media. *Transport in Porous Media* **146** (1), 55–84.
- MEUNIER, P. & VILLERMAUX, E. 2010 The diffusive strip method for scalar mixing in two dimensions. *J Fluid Mech.* **662**, 134–172.
- MOFFATT, H. K. 1969 The degree of knottedness of tangled vortex lines. *Journal of Fluid Mechanics* **1**, 117–129.
- MOREAU, JEAN JACQUES 1961 Constantes d’un ilot tourbillonnaire en fluide parfait barotrope. *Comptes Rendus Acad. Sci. Paris* **252**, 2810–2812.
- MOUSSAFIR, JACQUES-OLIVIER 2006 On computing the entropy of braids. *Functional Analysis and Other Mathematics* **1** (1), 37–46.
- NEUFELD, Z. & HERNANDEZ-GARCIA, E. 2009 *Chemical and biological processes in fluid flows: A dynamical systems approach*. Imperial College Press.
- NEUMAN, SHLOMO P. & ZHANG, YOU-KUAN 1990 A quasi-linear theory of non-fickian and fickian subsurface dispersion: 1. theoretical analysis with application to isotropic media. *Water Resources Research* **26** (5), 887–902.
- NEWHOUSE, SHELDON & PIGNATARO, THEA 1993 On the estimation of topological entropy. *Journal of Statistical Physics* **72** (5), 1331–1351.
- NEWHOUSE, SHELDON E. 1988 Entropy and volume. *Ergodic Theory and Dynamical Systems* **8**, 283–299.

- ÓDOR, GÉZA 2004 Universality classes in nonequilibrium lattice systems. *Rev. Mod. Phys.* **76**, 663–724.
- OTTINO, J. M. 1989 *The Kinematics of Mixing: Stretching, Chaos, and Transport*. Cambridge, United Kingdom: Cambridge University Press.
- OUELLETTE, NICHOLAS T, O'MALLEY, PJJ & GOLLUB, JERRY P 2008 Transport of finite-sized particles in chaotic flow. *Phys. Rev. Lett.* **101** (17), 174504.
- REBENSHTOK, ADI, DENISOV, SERGEY, HÄNGGI, PETER & BARKAI, ELI 2014 Non-normalizable densities in strong anomalous diffusion: Beyond the central limit theorem. *Phys. Rev. Lett.* **112**, 110601.
- RENARD, PH & DE MARSILY, G 1997 Calculating equivalent permeability: a review. *Advances in water resources* **20** (5-6), 253–278.
- ROBERTS, ERIC, SINDI, SUZANNE, SMITH, SPENCER A. & MITCHELL, KEVIN A. 2019 Ensemble-based topological entropy calculation (e-tec). *Chaos: An Interdisciplinary Journal of Nonlinear Science* **29** (1), 013124.
- ROLLE, MASSIMO & LE BORGNE, TANGUY 2019 Mixing and reactive fronts in the subsurface. *Reviews in Mineralogy and Geochemistry* **85** (1), 111–142.
- SAFFMAN, PG 1959 A theory of dispersion in a porous medium. *Journal of Fluid Mechanics* **6** (3), 321–349.
- SCHUTZ, BERNARD F. 1980 *Geometrical Methods of Mathematical Physics*. Cambridge University Press.
- SOUZY, M, LHUISSIER, H, MÉHEUST, Y, LE BORGNE, T & METZGER, B 2020 Velocity distributions, dispersion and stretching in three-dimensional porous media. *J. Fluid Mech* **891** (A16).
- SPEETJENS, MICHEL, METCALFE, GUY & RUDMAN, MURRAY 2021 Lagrangian Transport and Chaotic Advection in Three-Dimensional Laminar Flows. *Applied Mechanics Reviews* **73** (3), 030801.
- TAYLOR, G. I. 1953 Dispersion of soluble matter in solvent flowing slowly through a tube. *Philosophical Transactions of the Royal Society A: Mathematical, Physical and Engineering Sciences* **219**, 186–203.
- TÉL, TAMÁS, KÁROLYI, GYÖRGY, PÉNTÉK, ÁRON, SCHEURING, ISTVÁN, TOROCZKAI, ZOLTÁN, GREBOGI, CELSO & KADTKE, JAMES 2000 Chaotic advection, diffusion, and reactions in open flows. *Chaos: An Interdisciplinary Journal of Nonlinear Science* **10** (1), 89–98.
- TÉL, TAMÁS, DE MOURA, ALESSANDRO, GREBOGI, CELSO & KÁROLYI, GYÖRGY 2005 Chemical and biological activity in open flows: A dynamical system approach. *Physics Reports* **413** (2–3), 91 – 196.
- THIFFEAULT, JEAN-LUC 2005 Measuring topological chaos. *Phys. Rev. Lett.* **94**, 084502.
- THIFFEAULT, JEAN-LUC 2010 Braids of entangled particle trajectories. *Chaos: An Interdisciplinary Journal of Nonlinear Science* **20** (1), 017516.
- THIFFEAULT, JEAN-LUC 2022 *Braids and Dynamics*. Springer Cham.
- THIFFEAULT, JEAN-LUC & BUDIŠIĆ, MARKO 2013–2021 Braidlab: A software package for braids and loops. 3.2.5.
- THIFFEAULT, JEAN-LUC & FINN, MATTHEW D 2006 Topology, braids and mixing in fluids. *Philosophical Transactions of the Royal Society A: Mathematical, Physical and Engineering Sciences* **364**, 3251–3266.
- TREFRY, M. G., LESTER, D. R., METCALFE, G. & WU, J. 2019 Temporal fluctuations and poroelasticity can generate chaotic advection in natural groundwater systems. *Water Resources Research* **55** (4), 3347–3374.
- TURUBAN, RÉGIS, LESTER, DANIEL R, HEYMAN, JORIS, LE BORGNE, TANGUY & MÉHEUST, YVES 2019 Chaotic mixing in crystalline granular media. *Journal of Fluid Mechanics* **871**, 562–594.
- TURUBAN, RÉGIS, LESTER, DANIEL R, LE BORGNE, TANGUY & MÉHEUST, YVES 2018 Space-group symmetries generate chaotic fluid advection in crystalline granular media. *Physical Review Letters* **120** (2), 024501.
- VALOCCHI, ALBERT J, BOLSTER, DIOGO & WERTH, CHARLES J 2019 Mixing-limited reactions in porous media. *Transport in Porous Media* **130** (1), 157–182.
- VILLERMAUX, EMMANUEL 2012 Mixing by porous media. *Comptes Rendus Mécanique* **340** (11–12), 933 – 943, out of Equilibrium Dynamics.

- VILLERMAUX, EMMANUEL 2019 Mixing versus stirring. *Annu. Rev. Fluid Mech.* **51** (1), 245–273.
- VILLERMAUX, E. & DUPLAT, J. 2003 Mixing as an aggregation process. *Phys. Rev. Lett.* **91**, 184501.
- WOLTJER, L 1958 A theorem on force-free magnetic fields. *Proceedings of the National Academy of Sciences* **44** (6), 489–491.
- WRIGHT, ELISE E, RICHTER, DAVID H & BOLSTER, DIOGO 2017 Effects of incomplete mixing on reactive transport in flows through heterogeneous porous media. *Physical Review Fluids* **2** (11), 114501.
- WU, JUNHONG, LESTER, DANIEL, TREFRY, MICHAEL G. & METCALFE, GUY 2024 Lagrangian coherent structures control solute dispersion in heterogeneous poroelastic media. *Phys. Rev. Fluids* **9**, 044501.
- WU, J., LESTER, D. R., TREFRY, M. G. & METCALFE, G. 2020 When do complex transport dynamics arise in natural groundwater systems? *Water Resources Research* **56** (2), e2019WR025982.
- YE, YU, CHIOGNA, GABRIELE, CIRPKA, OLAF A., GRATHWOHL, PETER & ROLLE, MASSIMO 2015 Experimental evidence of helical flow in porous media. *Phys. Rev. Lett.* **115**, 194502.
- YOMDIN, Y. 1987 Volume growth and entropy. *Israel Journal of Mathematics* **57** (3), 285–300.
- YOSHIDA, Z. 2009 Clebsch parameterization: Basic properties and remarks on its applications. *Journal of Mathematical Physics* **50** (11), 113101.
- YOSHIDA, Z. & MORRISON, P. J. 2017 Epi-two-dimensional fluid flow: A new topological paradigm for dimensionality. *Phys. Rev. Lett.* **119**, 244501.